

The Use of Impedance Spectroscopy in Characterizing Low Voltage
Electrowetting-on-dielectric

A Dissertation

Presented to
the faculty of the School of Engineering and Applied Science
University of Virginia

in partial fulfillment
of the requirements for the degree

Doctor of Philosophy

by

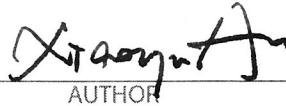
Xiaoyu Hu

December

2016

APPROVAL SHEET

The dissertation
is submitted in partial fulfillment of the requirements
for the degree of
Doctor of Philosophy



AUTHOR

The dissertation has been read and approved by the examining committee:

Michael L. Reed

Advisor

N. Scott Barker

Carl Knospe

Giovanni Zangari

Nathan Swami

Accepted for the School of Engineering and Applied Science:



Craig H. Benson, Dean, School of Engineering and Applied Science

December
2016

Abstract

Being able to control fluid shape and flow using an external electric field alone without any mechanical parts, electrowetting-on-dielectric (EWOD) has drawn a lot of attention from researchers which leads to the the invention of many interesting applications. In the laboratory, EWOD characterization is generally conducted using direct optical observation of the droplet. While being a straight-forward method, optical techniques are laborious, slow, subject to optical distortions, and impractical in devices where the electrowetted droplet is a functional part of a larger system. In such cases, having an integrated means to interrogate the droplet configuration quickly and accurately would be highly desirable. As most EWOD experimental setups/devices have a metal-insulator-metal structure, it is possible to characterize the wetting process using electrical measurements. Prior efforts in characterizing EWOD electrically exhibit limitations in: 1) the dielectric layer used were relatively thick; 2) overly simplistic assumptions were made regarding the droplet shape. Because electrical characterization of EWOD is beneficial in many ways, we have investigated methods to expand its use and increase its flexibility so it could be applied to various kinds of experiments and applications. In this work, we first experimentally investigated the impedance of various EWOD configurations as a function of frequency, helping researchers to develop a framework for characterizing the impedance of an EWOD experiment using electrode properties and material parameters. Secondly, we developed methods to use electrical measurements in conjunction with known capillary bridge geometries to accurately determine unknown parameters in electrowetting (e.g., contact angle, liquid volume, interfacial tension, etc.). Lastly, we designed, built, and tested a capacitance measurement system capable of high-speed time-resolved measurements of electrowetting behavior.

Acknowledgement

First and foremost, I would like to give my sincere gratitude to my academic advisor Prof. Michael Reed, for his continuous guidance, support, and encouragement during my Ph.D. study. Coming to the States as a fresh college graduate with little experiences in doing experiments, it had been challenging for me at the beginning. While Prof. Reed has always been very patient and kind, helping me go through all those difficulties by answering tons of my "stupid" questions and sharing with me many interesting stories. I have learned so much from him and it has always been so much fun talking to him.

I would also like to thank Prof. Carl Knospe, for his many help and inspirations during my study. He has always been so willing to help us solve detailed research problems and discuss about solutions and ideas. This dissertation would not have been possible without his valuable help and support. I also sincerely appreciate the valuable advice and generous help from other members of my Ph.D. committee: Prof. Giovanni Zangari, Prof. Scott Barker, and Prof. Nathan Swami.

Besides, I truly appreciate the numerous help I received from the staff members at the Microfabrication Lab: Joe Beatrice, Alex Lobo, Michael Stogoski, Jian Zhang, and Jie Wang. They have been very generous to offer help with various instrument problems I encountered. I would also like to sincerely acknowledge the assistance from Beth A. Eastwood-Beatty, Daniel Fetko, Susan Malone, and Yadira Weaver.

In addition, I would like to thank Vivian Ji and Huihui Wang for their help in my early years here. I am very grateful for having the chance to spend five years of my life in the beautiful Charlottesville and meet all the new friends including my fellow group members: Marcel Mibus, Christina Barth, Samantha Mendis, Nicholas Francis, and Wilson Ruotolo.

Finally, I would like to thank my family for their unconditional love and support. To mom and dad: you have always been the coolest parents I have seen and I am so lucky to have you; and to my husband He Qi: thanks for being my best friend.

This work is partially supported by NSF Grant CMMI 1030868.

List of Figures

1	Top: A water drop place on a hydrophobic surface with a high contact angle. Bottom: Electrowetting of the surface. [2]	1
2	LY curve.	3
3	(a) Schematic representation and sample photograph of a lens of variable focal length; (b) Inverse focal length of a particular lens of 6 mm diameter, filled with -chloronaphtalene as the insulating liquid, and a Na ₂ SO ₄ solution in water, as a function of voltage. [6]	5
4	(a) An array of liquid-metal droplets on a digital-microfluidic chip; (b) temperature profile of a hot spot as a mercury droplet passes over it. [18]	6
5	Illustration of an example experiment scheme with FT A contact angle measurement system. [25]	7
6	(a) Schematic drawing of a capacitance-based contact-angle measurement, and (b) derived contact angle as a function of voltage. [26] . . .	9
7	(a) Top view of a droplet aligned with dielectric covered electrode element, and (b) expected capacitance vs. droplet volume. [27]	10
8	Most common configurations in EWOD experiments. U is the applied bias. Black and gray areas represent conducting and dielectric layers, respectively.	14
9	(a) Experimental setup; (b) equivalent circuit; (c) impedance magnitude (left) and phase (right) spectra for two gold wires immersed in Na ₂ SO ₄ solutions with concentration of 0.005M (red), 0.05M (blue), and 0.5M (green).	16
10	Parameter fitting for two gold wires immersed in 0.5 M Na ₂ SO ₄ solution.	18
11	Experimental setup for testing planar electrode/liquid interface. . . .	20

12	Experimental impedance and fitted model (0.5M Na ₂ SO ₄).	20
13	(a) Experimental setup; (b) equivalent circuit for the planar dielectric/ liquid interface test.	21
14	(a) Impedance magnitude and (b) phase spectra and (c) reactance spectra for Cytop coated ITO slides in contact with a 0.5M Na ₂ SO ₄ liquid drop. Curves in various colors represent tests with different contact areas; "d" in the legend denotes the contact circle diameter. . .	22
15	Typical impedance spectra and model impedance for Cytop coated ITO slides in contact with a 0.5M Na ₂ SO ₄ liquid drop.	24
16	Measured C-V result for a parallel plate EWOD setup with the droplet pinned on both sides with the dielectric being: (a) a bilayer composed of a 43 nm aluminum oxide layer topped by a 17 nm Cytop hydrophobic layer; (b) a single 457 nm Cytop layer.	29
17	Experimental setup: Parallel plate configuration with the liquid bridge pinned on lower surface and electrowetting on upper surface.	33
18	Electrical impedance model of experimental setup.	33
19	(a) Measured C-V result and (b) calculated radius of wetted area (r_u).	38
20	Contact angle calculated by Approach I as a function of bias voltage. Also shown is LY curve determined from oil/ electrolyte surface tension and layer dielectric properties.	43
21	Liquid/ambient interfacial tension σ calculated by Approach II as a function of bias voltage.	45
22	Droplet volume calculated by Approach III as a function of bias volt- age. Also shown is the experimental drop volume (4.20 μ L) specified by the pipette dispenser.	47

23	Standard deviation of calculated drop volume as a function of the assumed initial contact angle.	48
24	Standard deviation of calculated drop volume as a function of the assumed initial contact angle and surface tension. The calculated minimum point (26.5, 165) and the true parameter values (16.9, 150) are also shown.	50
25	Standard deviation of calculated drop volume as a function of the assumed initial contact angle and surface tension for the hypothetical experiment. The calculated minimum point (16.9, 150) is also shown.	52
26	Circuit schematic of the custom-built capacitance measurement system.	58
27	Oscilloscope capture of a 0-10V voltage step generated by the HP3631A DC power supply.	59
28	TI TMS320F28377S eCAP module capture sequence for delta mode time-stamp and rising edge trigger. [59]	62
29	Interconnection schematic between the TMS320F28377S micro-controller and SD card in SPI mode.	63
30	Actual interconnection between the TMS320F28377S micro-controller and SD card.	64
31	Software design flow for frequency measurement and data acquisition.	65
32	Capacitance-time data in response to a 0-7V and 7-0 V step input. Each data point is the average of ten capacitance measurements.	68
33	Drop radius change during the transient determined from the measured capacitance data.	69
34	Radial speed of the contact line calculated from the fitted model for radius change.	69
35	Measurement speed and capacitance resolution as a function of V_1	71

List of Tables

1	Fitted parameters for the wire electrode/liquid interface experiments.	19
2	Analytical expression of the Plateau sequence.	40
3	Illustrative profiles for axisymmetric bridges with unequal contact angles.	41
4	A list of IC components used in the capacitance measurement circuit.	60

Contents

1	Introduction	1
1.1	Low-voltage Electrowetting-on-dielectric	1
1.2	EWOD Applications	4
1.3	EWOD Characterization Methods	7
1.4	Thesis Goal and Organization	12
2	Impedance Spectroscopy and Electrical Modeling of EWOD Devices	13
2.1	Introduction	13
2.2	Setup Design, Measurement, Modeling, and Analysis	13
2.2.1	Materials and Experimental Setup	14
2.2.2	Wire Electrode/Liquid Interface	15
2.2.3	Planar Electrode/Liquid Interface	20
2.2.4	Dielectric/Liquid Interface	21
2.3	Impedance of Typical EWOD Arrangements and Implications for Area Determination	25
2.3.1	EWOD with Wire Electrode	25
2.3.2	EWOD with Planar Electrode	27
2.3.3	EWOD with Insulated Electrode	28
2.3.4	Invariance with Varying Bias	28
2.4	Conclusion	31
3	Interrogation of Droplet Configuration	32
3.1	Introduction	32
3.2	Experiments	32
3.2.1	Approaches	32

3.2.2	Materials and Fabrication	34
3.2.3	Electrowetting and Impedance Spectroscopy	35
3.2.4	Dominance of Dielectric Layers Impedance	35
3.3	Results and Discussion	38
3.3.1	Capacitance-Voltage Results	38
3.3.2	Modeling Theory and Method	38
3.3.3	Problem I: Find the Contact Angle	42
3.3.4	Problem II: Find the Surface Tension	43
3.3.5	Problem III: Find the Drop Volume	46
3.3.6	Problem IV	47
3.4	Conclusion	53
4	Building a High-speed Capacitance Measurement System for Characterizing Dynamic EWOD	54
4.1	Introduction	54
4.2	Circuit Design	56
4.3	Frequency Measurement and Data Acquisition	61
4.3.1	Frequency Measurement	61
4.3.2	Data Acquisition	62
4.4	Results and Analysis	67
4.5	Evaluation of the Measurement System	70
5	Conclusion and Future Work	73
5.1	Impedance Spectroscopy of EWOD Devices	73
5.2	Interrogation of Droplet Configuration	74
5.3	High-speed Capacitance Measurement System	75

Appendices	84
Appendix A <code>main.c</code>	84
Appendix B <code>mmc.c</code>	87
Appendix C <code>datatranslate.py</code>	101

1 Introduction

1.1 Low-voltage Electrowetting-on-dielectric

Electrowetting-on-dielectric (EWOD) is a phenomenon where a voltage applied to a conducting liquid on a dielectric covered electrode causes the liquid to spread over the dielectric surface. [1] Figure 1 illustrates the electrowetting of a water droplet on a dielectric coated electrode. With the application of a voltage, the electric charges in the liquid drop move and concentrate in different locations of the drop and the forces working on the charges lead to the flattening out of the drop.

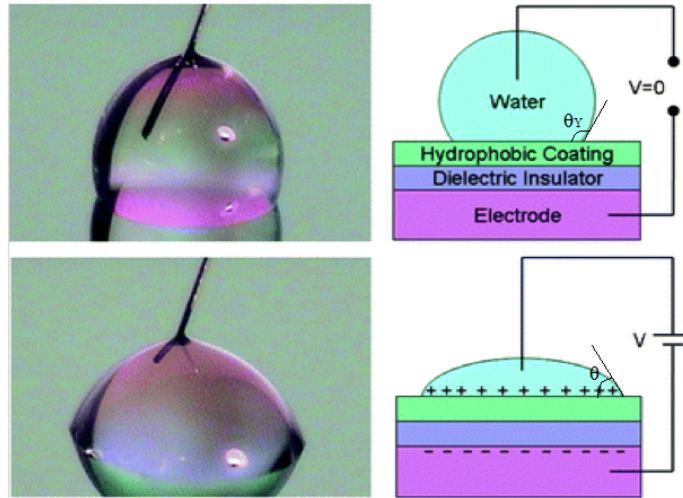


Figure 1: Top: A water drop place on a hydrophobic surface with a high contact angle. Bottom: Electrowetting of the surface. [2]

The relationship between the wetting angle and applied voltage is described by the Lippmann-Young (LY) equation:

$$\cos \theta = \cos \theta_Y + \frac{1}{2\sigma_{lv}} c_H V^2 = \cos \theta_Y + \frac{\epsilon_0 \epsilon_r}{2t\sigma_{lv}} V^2, \quad (1)$$

where θ is the apparent contact angle (the mesoscopic contact angle, shown in Figure 1), θ_Y is the Young's equilibrium contact angle with no applied field (shown in Figure

1), σ_{lv} is the liquid-vapor interface tension, V is the applied bias across the dielectric layer, and $c_H = \varepsilon_0\varepsilon_r/t$ is the dielectric capacitance per unit area. Here ε_0 is the vacuum permittivity, ε_r is the dielectric constant, and t is the dielectric thickness. Note that for devices with two or more dielectric layers, such as that shown in Figure 1, c_H is the series combination of each dielectric capacitance and equivalent values should be used for ε_r and t .

Two typical LY curves describing the relation between contact angle and bias are drawn in Figure 2. Parameters used in calculating the contact angle change are: initial angle $\theta_Y = 110^\circ$, dielectric permittivity $\varepsilon_r = 2.1$ (hydrophobic Cytop), and interface tension $\sigma_{lv} = 72mN/m$ (water-air interface). Two values are used for dielectric thickness: the blue curve is plotted with $t = 500nm$ and the green is plotted with $t = 50nm$. It can be seen that devices with thinner dielectric layers are capable of achieving a much more significant wetting effect with the same applied bias voltage. Yet in the majority of commercial and lab EWOD devices, dielectric layers are generally at least one to ten micrometers thick, which would require an excess level of applied voltage to achieve appreciable contact angle change. For many EWOD applications, this implies difficulty to be integrated into integrated circuit (IC) chips since such high voltages are incompatible with modern IC technologies. Therefore, it is worthwhile exploring the use of thin dielectric layers in EWOD devices.

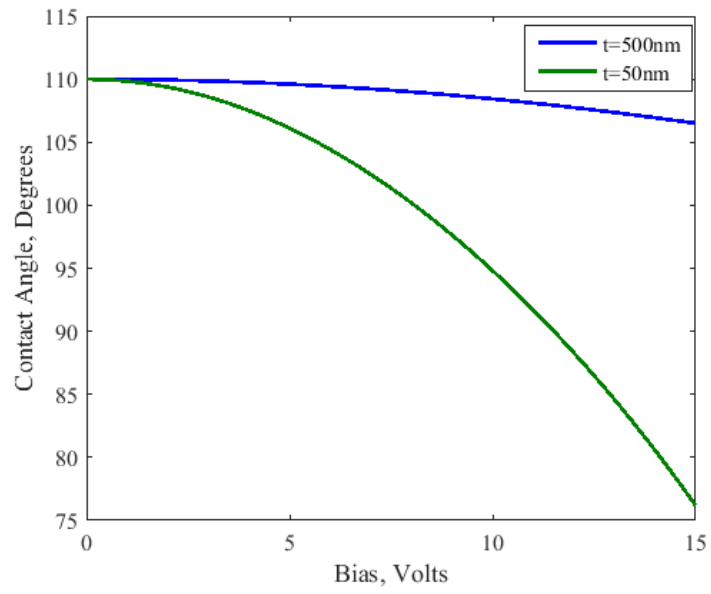


Figure 2: LY curve.

1.2 EWOD Applications

First discovered in Lippmann's (1875) [3] and Froumkin's (1936) [4] time, electrowetting was conducted with electrolyte directly placed on electrodes. However, the application of the voltage at the electrolyte/metal interface led to inevitable electrochemical reactions, which, over time, led to irreversible changes of the interface. This greatly limits electrowetting's application prospects as applications normally require many cycles of on/off or wetting/dewetting. Later on, the solution to this problem was found by adding a dielectric layer between the metal electrode and the liquid drop [5] and is named as electrowetting-on-dielectric (EWOD). As the electrochemical reactions between the electrode and electrolyte are now prevented, electrowetting can operate stably for a much longer period of time.

Being able to control fluid shape and flow using an external electric field alone without any mechanical parts, EWOD has drawn a lot of attention from researchers which leads to the invention of many interesting applications. Berge and Peseux [6] used electrocapillarity to change the contact angle of a transparent drop (1-bromododecane immersed in a solution of Na_2SO_4 in water) and achieved a lens of variable focal length (Figure 3). The optical power variation was 5-10 times that of the human eye for a comparable diameter. The typical response time was 0.03 s and the dissipated power was only a few mW. Some other works demonstrating EWOD based variable-focus liquid lens can be found in [7–10].

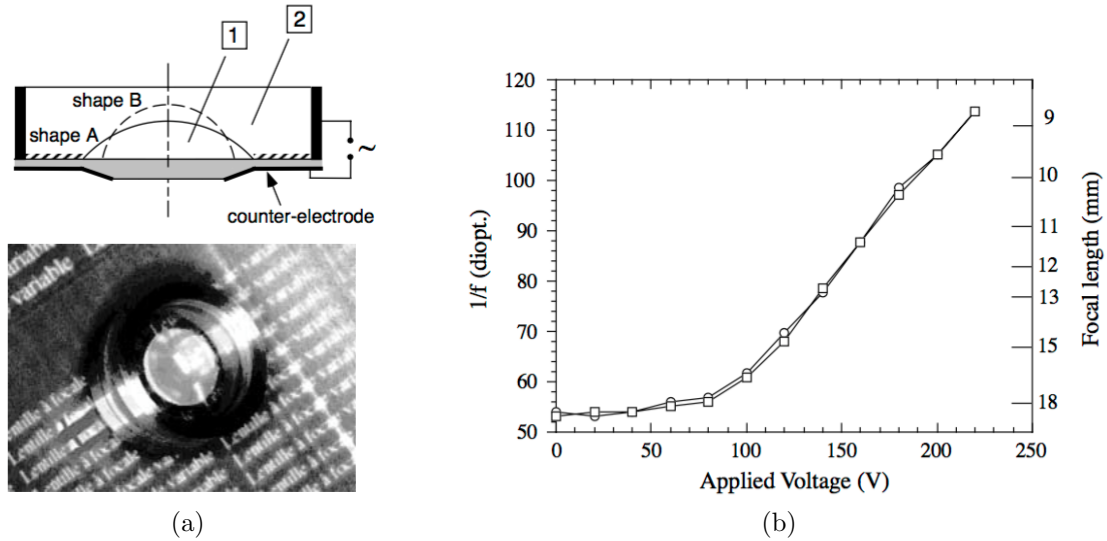


Figure 3: (a) Schematic representation and sample photograph of a lens of variable focal length; (b) Inverse focal length of a particular lens of 6 mm diameter, filled with -chloronaphtalene as the insulating liquid, and a Na₂SO₄ solution in water, as a function of voltage. [6]

EWOD also find its application in microfluidic field based on the actuation of droplet volumes up to several microliters [11]. Applications including area-tunable micromirror [12], dynamically tuned optical waveguides [13], fast microfluidic mixing [14], liquid transport/mixing/splitting for biomedical applications [15–17], etc. have been proposed and tested. EWOD based digital microfluidic architecture is advantageous in real applications in that: there is no need for moving parts or channels; many droplets can be independently controlled; sample heating is minimized as there is no ohmic current; it works with various liquids; it is energy efficient and fast [11].

Paik and Chakrabarty [18] reported on applying EWOD based digital-microfluidic architectures to Integrated Circuits (IC) chip cooling (Figure 4). Liquid drops formed from reservoirs of cooling liquid were sandwiched between the IC chip and a digital-microfluidic chip. They could move in reconfigurable paths and bring away heat from hot spots. An additional active-cooling device was attached to the microfluidic chip to further dissipate the heat. Using aqueous or liquid-metal droplets to facilitate IC

cooling is beneficial in that it has the ability to rapidly respond to changing cooling demands. Similar works can be found in [19–22].

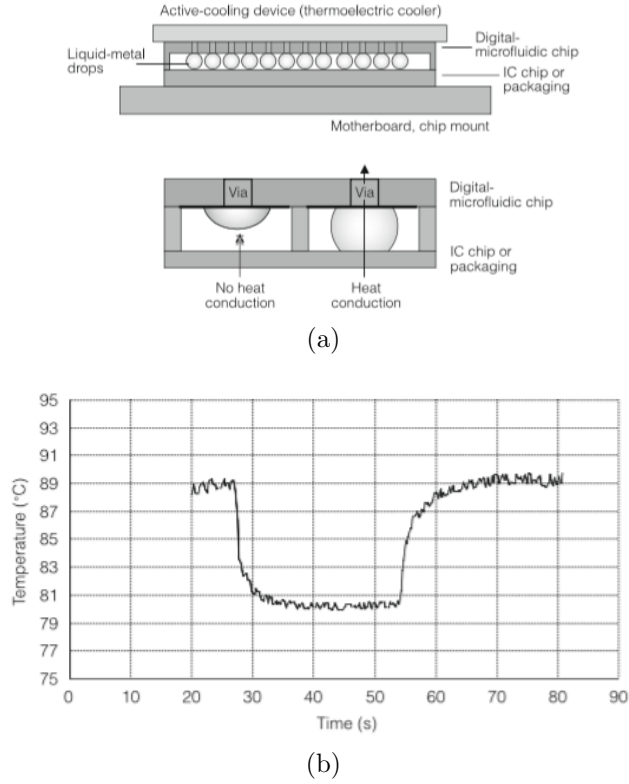


Figure 4: (a) An array of liquid-metal droplets on a digital-microfluidic chip; (b) temperature profile of a hot spot as a mercury droplet passes over it. [18]

Another interesting application of EWOD is electronic paper (e-paper) and electrowetting display. Researchers have successfully created thin display surfaces suitable for portable electronic devices that operate in video-speed [23,24]. EWOD based displays reflect light instead of emitting light, which is less tiring and healthier for human eyes. In addition, they tend to have a wider viewing angle compared to light-emitting LCD displays.

1.3 EWOD Characterization Methods

In the laboratory, EWOD characterization is generally conducted using direct optical observation of the droplet. This is often a straight-forward method that gives direct measurement of the contact angle, thus has long been used for characterizing EWOD performance in the lab.

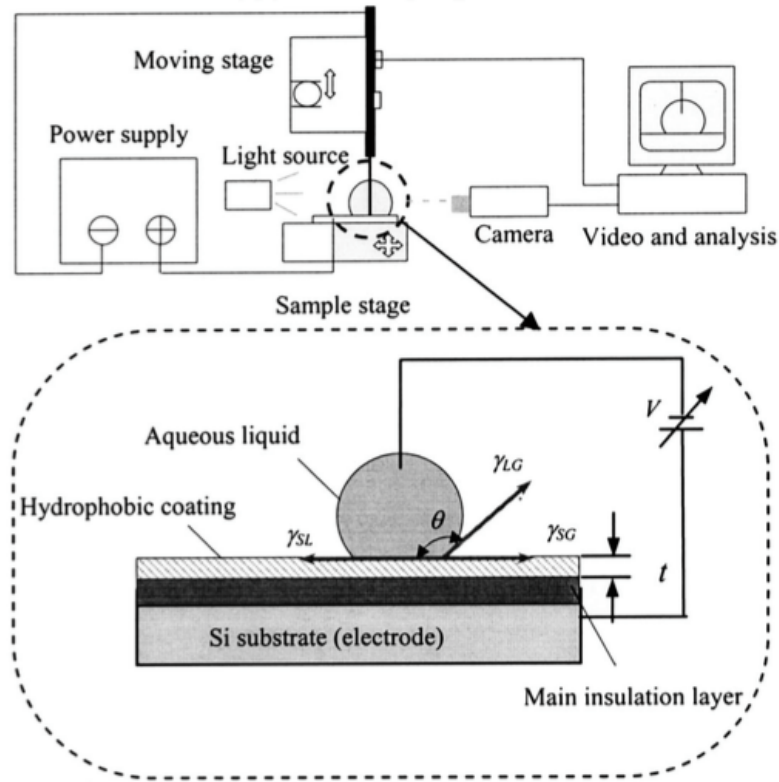
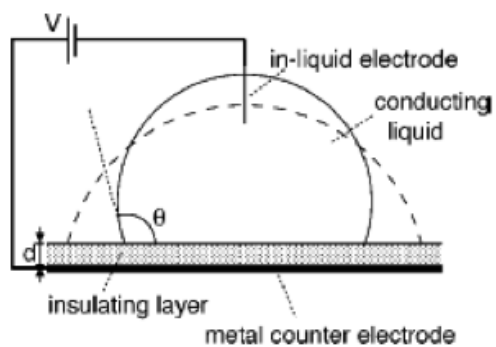


Figure 5: Illustration of an example experiment scheme with FT A contact angle measurement system. [25]

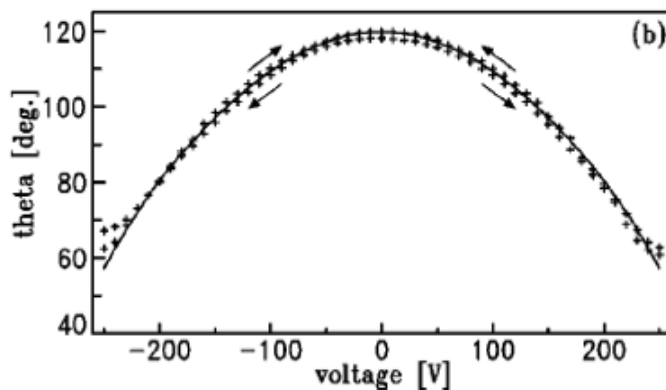
While being a straight-forward method, optical techniques are laborious, slow, and subject to optical distortions, which makes it difficult to characterize EWOD configuration or devices where the droplet is sandwiched between two parallel planar electrodes. In addition, optical methods are impractical in devices where the electrowetted droplet is a functional part of a larger system because of the size, cost, and

complexity of imaging systems. In such cases, having an integrated means to interrogate the droplet configuration quickly and accurately would be highly desirable.

Most EWOD experimental setups/devices have a metal-insulator-metal structure comprising of a conductive electrolyte drop on an insulating dielectric layer covered flat electrode, making it possible to characterize the wetting process using capacitance measurements. An early report of this was made by Verheijen and Prins from the Philips Research Laboratories, who measured the LY curve with the traditional EWOD sessile drop configuration (Figure 6) via capacitance measurements in 1999 [26]. As the dielectric layer used was relatively thick ($10\ \mu\text{m}$), the measured capacitance was seen as a direct reflection of the wetted area. Assuming that the $10\ \mu\text{L}$ liquid droplet in air ambient had maintained the shape of a spherical cap, the contact angle was derived geometrically. The result was in good agreement with electrowetting theory.



(a)



(b)

Figure 6: (a) Schematic drawing of a capacitance-based contact-angle measurement, and (b) derived contact angle as a function of voltage. [26]

Over the next few years, a number of groups [27–31] reported on EWOD-based microfluidic systems. In their works, EWOD was used to realize or control processes like on-chip droplet dispensing, moving, merging, or splitting. During these steps, droplet position and volume are critical parameters that define the accuracy and reliability of the systems, especially for safety-critical biomedical applications. In their works, simple RC oscillator circuits were utilized to sense the capacitance change as droplets moved over individual elements of the electrode array (Figure 7) or were deposited on the substrate. Droplet volume was estimated by assuming a cylindrical shape for the drop sandwiched between parallel electrodes. In these microfluidic systems, electrical measurement is highly advantageous as it provides an integrated

way of characterizing device performance.

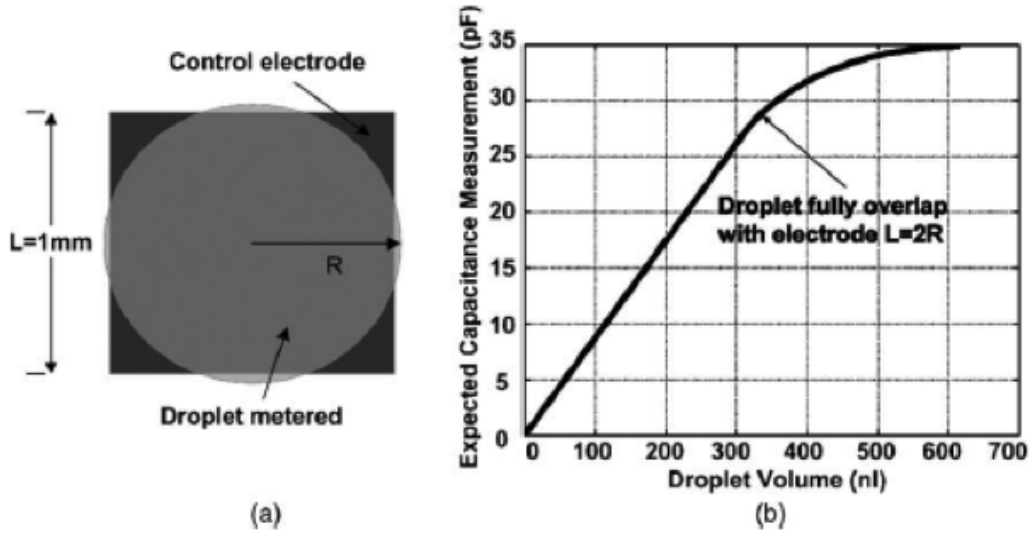


Figure 7: (a) Top view of a droplet aligned with dielectric covered electrode element, and (b) expected capacitance vs. droplet volume. [27]

However, these existing works exhibit some limitations:

- The dielectric layer used were relatively thick ($\sim\mu\text{m}$). Current devices scaled down and dielectric layers are much thinner ($\sim\text{nm}$). Thinner dielectrics brings the benefit of achieving the same wetting effect with a much lower bias, it also results in a great change in the impedance of the dielectric layer and its proportion of the total impedance of the system.
- Overly simplistic assumptions were made regarding the droplet shape. There are many different kinds of device structures, especially in practical applications:
 - (1) Electrodes can be flat or sharp as well as dielectric covered or bare;
 - (2) contact lines can be pinned on one electrode or free to move on both electrodes;
 - (3) contact angle ranges from as high as $\sim 160^\circ$ to as low as $\sim 20^\circ$. In such cases, the droplet shape can be far away from a simple spherical cap or cylinder.

Because electrical characterization of EWOD is beneficial in many ways, we have

investigated methods to expand its use and increase its flexibility so it could be applied to various kinds of experiments and applications.

1.4 Thesis Goal and Organization

The primary focus of this work is to study the application of electrical measurements in characterizing thin-film low-voltage EWOD. Compared to traditional optical characterization method, which is laborious and expensive, impedance spectroscopy measurement uses the present electrical contacts and is easier, faster, and more accurate. Throughout the study, various thin-film EWOD devices were fabricated and tested; electrical models were proposed and verified; experiments and mathematical simulations were combined to explore what electrical measurement could do to facilitate the characterization and understanding of low-voltage EWOD.

This dissertation consists of five chapters:

- Chapter 1 introduces the fundamentals of EWOD, reviews the current characterization method, and analyzes its advantages and disadvantages.
- Chapter 2 discusses the measurement and analysis of the impedance spectra of various electrowetting setups and generates comprehensive guidelines useful for electrical characterization of electrowetting systems.
- Chapter 3 applies the impedance spectroscopy method to thin-film EWOD devices and achieves high-precision droplet configuration (contact angle, droplet volume, surface tension, etc.) identification with droplet meniscus modeling.
- Chapter 4 builds a mixed signal circuit board capable of high-speed capacitance measurement useful for characterizing dynamic EWOD.
- Chapter 5 concludes the current study and suggests possible future work.

2 Impedance Spectroscopy and Electrical Modeling of EWOD Devices

2.1 Introduction

As mentioned in the previous chapter, setups with thin layers can have very different impedance spectra. As a first step, we measured the Capacitance-Voltage (C-V) response of the most commonly seen EWOD setup similar to the one in Figure 6a. The only difference is that the dielectric layer was thinner by more than two orders of magnitude (~ 30 nm compared to ~ 10 μm). Although electrowetting phenomenon was confirmed visually, the measured C-V curve was rather random and not repeatable. To understand this behavior and to answer the question can we characterize thin-film EWOD devices electrically and how can we do it question, the first step is to analyze the electrical behaviors of various elements appearing in the devices.

2.2 Setup Design, Measurement, Modeling, and Analysis

Three electrode arrangements are commonly seen in EWOD experiments and applications. These arrangements, shown in Figure 8, are: (a) a sessile droplet placed upon a dielectric covered planar electrode with a metal wire inserted into the drop as the counter electrode; (b) a liquid drop sandwiched between two parallel plates, a bare electrode and a dielectric covered electrode; and (c) a parallel electrode configuration similar to (b) except that both of the electrodes are covered with dielectric layers. To achieve a thorough understanding of the electrical properties of these EWOD systems and the potential for electrically characterizing droplet configuration, we have experimentally examined the impedance spectra of each of the interface elements that appear in Figure 8 and have developed equivalent circuit models. The

experiments that we present were all designed so that no electrowetting would occur during impedance measurement. This allows the wetted area in each case to be independently controlled from the electrical bias used and to be precisely measured.

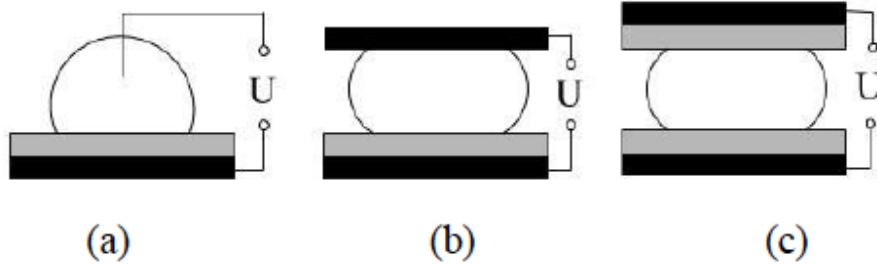


Figure 8: Most common configurations in EWOD experiments. U is the applied bias. Black and gray areas represent conducting and dielectric layers, respectively.

2.2.1 Materials and Experimental Setup

Electrodes used in our tests include gold bonding wires, gold plates, and indium tin oxide (ITO) coated glass slides. The gold wire was $25\ \mu\text{m}$ in diameter, sufficiently small to have little influence on droplet shape when inserted. The contact area between the gold and the liquid was controlled by partially coating the wire with a thick insulating layer of nitrocellulose. Planar electrodes were fabricated on silicon wafers by depositing a 100 nm thick gold layer using an electron beam evaporator. All samples were cleaned using standard micro-fabrication cleaning procedures to minimize surface contamination. The ITO coated glass slides (30-60 nm thick ITO, obtained from Sigma Aldrich) had an optical transmittance greater than 84%, allowing the verification of the wetted area through direct optical observation.

The dielectric was a hydrophobic fluoropolymer, Cytop CTL-809M, supplied by Asahi Glass. The Cytop was diluted to a 1wt% solution by mixing with solvent CT-Solv.180, and was deposited on planar electrodes by spin-coating (2000 rpm, 30 seconds). In our experiments, multiple spin depositions were employed to achieve

the desired thickness. A short-duration, low-temperature partial drying step was carried out at 90°C for 15 minutes before applying the next layer. A one hour final cure at 160°C was employed to fully remove the remaining solvent, which improves layer adhesion to the substrate and reduces pinholes and defects intrinsic to the fluoropolymer material [37].

The impedances were measured using an HP 4192A Impedance Analyzer. The test signal consisted of a zero DC bias voltage with a small AC perturbation. The instrument has a full frequency range of 5 Hz to 13 MHz and a full oscillation level of 5 mV to 1.1 V. To achieve a better resolution of the measured results and to guarantee that the test AC signal does cause any EWOD effect, a nominal frequency range of 1 kHz to 13 MHz and a perturbation level of 10 mV were chosen. With the frequency range and perturbation level of our choice, the instrument is capable of achieving a resolution better than 0.1% of the full-scale range. Multi-strand Litz wires were used to connect the sample to the instrument to reduce the parasitic resistance from the leads arising from the skin effect at high frequencies [38].

2.2.2 Wire Electrode/Liquid Interface

The first experiment examined the impedance of a dual gold wire / electrolyte solution interface.

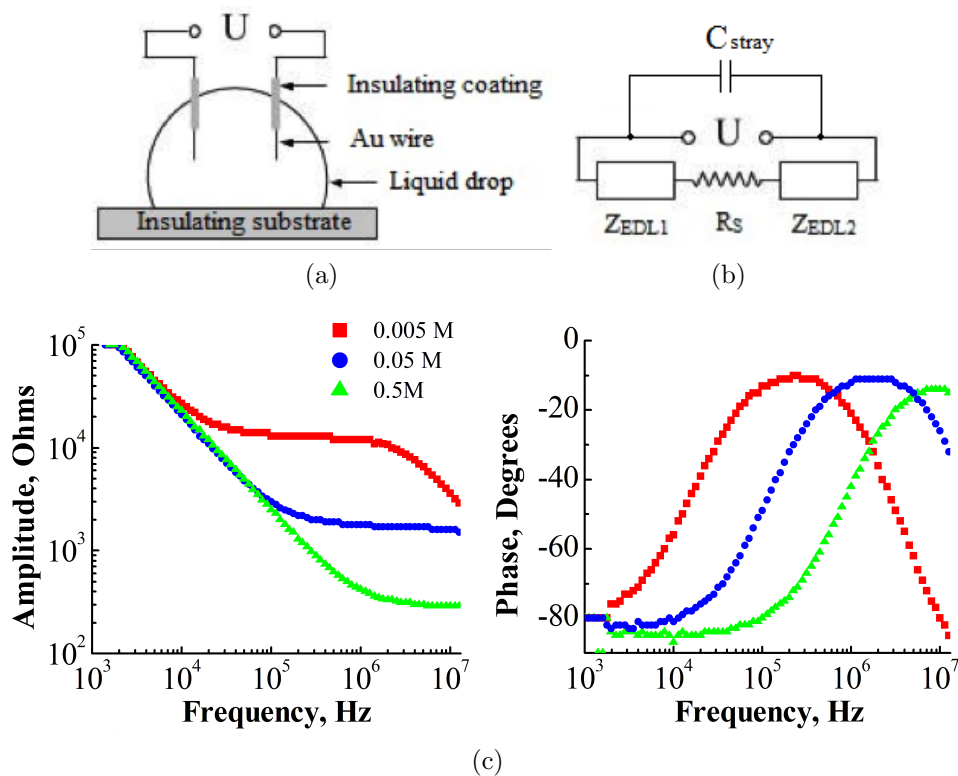


Figure 9: (a) Experimental setup; (b) equivalent circuit; (c) impedance magnitude (left) and phase (right) spectra for two gold wires immersed in Na_2SO_4 solutions with concentration of 0.005M (red), 0.05M (blue), and 0.5M (green).

As is shown in Figure 9a, the experimental setup consists of two partially insulated Au wires inserted into a sessile drop of x mol/L Na_2SO_4 solution ($x = 0.005, 0.05, 0.5$). The length of the bare wire segments was about $800 \mu m$. Typical impedance spectroscopy results are shown in Figure 9c for three different solution concentrations. In each curve the double layer capacitance is dominant at low frequencies, yielding a phase close to -90° and a magnitude slope of -1 decade per decade of frequency. Over the middle and high range of frequencies the impedance is dominated by the droplet resistance, where the phase approaches 0° and the magnitude curve has zero slope. The decrease in phase at very high frequencies (and corresponding fall in impedance magnitude) is due to the stray capacitance of the test fixture and instrument leads.

The stray capacitance, which is effectively in parallel with the device under test, is very small, typically a few pF. Such a small capacitance yields a parallel stray impedance orders of magnitude greater than the device impedance at low frequencies. The measured impedance is therefore dominated by the device impedance over much of the frequency range examined, since the smaller impedance largely determines the total impedance in a parallel circuit. At high frequencies, however, the stray impedance is much smaller as it is inversely proportional to frequency. For electrolytes having a larger bulk resistance (i.e., lower concentration) the stray impedance then becomes non-negligible at high frequencies, causing the phase to decrease towards -90° . The equivalent circuit representing the system (ignoring the stray impedance) is a series combination of the electric double layer (EDL) impedance at the electrode/electrolyte interface Z_{EDL1} , the resistance of the bulk electrolyte solution R_S , and the electric double layer impedance at the counter-electrode/electrolyte interface Z_{EDL2} in Figure 9b. The total impedance Z is thus

$$Z = Z_{EDL1} + R_S + Z_{EDL2} \quad (2)$$

The EDL is a specific interfacial region formed when an electrode is exposed to an electrolyte solution [32]. Its concept visualizes the ionic environment in the vicinity of a charged surface. Ideally, the electric double layer elements exhibit capacitive behaviors in the absence of Faradaic processes. In our experiments, however, the double layer invariably behaves like a CPE, where the impedance can be described by a power-law function of frequency [33]:

$$Z_{EDL}(\omega) = K(j\omega)^{-\alpha} \quad (3)$$

The CPE model describes the frequency dependence of the double layer impedance

observed in electrochemical experiments; empirically, the exponent α is in the range $0 < \alpha < 1$. When $\alpha = 1$, the impedance reduces to that of an ideal capacitor whose capacitance is K^{-1} . Current models for the origin of CPE behavior focus on two mechanisms: (1) the rough surface (with a porous or fractal geometry) of the electrode alters the effective solution resistance, which, combined with a uniform double layer capacitance, results in a phase angle independent of frequency; [34] (2) current density inhomogeneity caused by the atomic scale inhomogeneity of the electrode surface acting jointly with kinetic process such as phase transition and anion adsorption. [35]

Numerical values of the parameters K and α in the equivalent circuit were found by fitting the model to the experimental data using a multidimensional nonlinear minimization technique. Figure 10 shows the experimental magnitude and phase data and the corresponding fitted result for the test using the 0.5 M Na_2SO_4 solution. The stray element is also included in the fitting to account for the impedance at high frequencies. Fitted parameters are: $\alpha = 0.95$, $K = 4.10 \times 10^8 \Omega (\frac{\text{rad}}{\text{s}})^\alpha$, $R_S = 293 \Omega$.

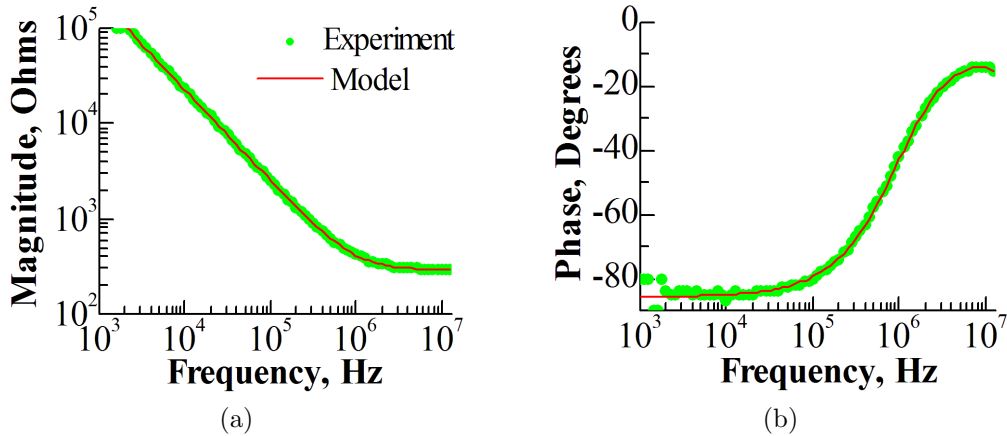


Figure 10: Parameter fitting for two gold wires immersed in 0.5 M Na_2SO_4 solution.

In order to correctly model and predict the electrical behaviors of the EDL element at the electrode/ electrolyte interface, the CPE model must be used instead

of a first order RC model. Yet since the CPE power parameter α is close to unity in our experiments, the K parameter should correlate to the EDL capacitance and the contact area to some extent. In this experiment, the wire electrode/ electrolyte interface has an area of $\sim 10^{-4}$ cm² (note that the wire length is ~ 800 μ m and wire diameter is ~ 25 μ m). Taking the EDL thickness t_{EDL} to be 0.7 nm and the EDL dielectric constant ε_{r_EDL} to be 6 [36], the EDL capacitance is calculated to be $C_{EDL} = \frac{\varepsilon_0 \varepsilon_{r_EDL} A_{EDL}}{t_{EDL}} \sim 10^{-8}$ F, which is on the same order of magnitude with the fitted parameter K^{-1} . Therefore, although a simple capacitor model is not able to describe the electrical behaviors of the EDL element precisely, it is capable of providing a rough estimation of the EDL impedance. The same values of parameters K and α also provide good fitting of the test data for the 0.05M and 0.005M Na₂SO₄ solutions. The fitted parameters for measurements with solutions of different molarities are listed in Table 1. Here the performance index “rval” is calculated as

$$rval = \sum_{f=1kHz}^{13MHz} \left(\frac{R_{exp} - R}{A_{exp}} \right)^2 + \sum_{f=1kHz}^{13MHz} \left(\frac{X_{exp} - X}{A_{exp}} \right)^2, \quad (4)$$

where R_{exp} , X_{exp} , and A_{exp} are the resistance, reactance, and amplitude of the measured impedance, and R , X , and A are those of the modeled impedance.

Table 1: Fitted parameters for the wire electrode/liquid interface experiments.

Molarity(M)	$K(\Omega(\frac{rad}{s})^\alpha)$	α	$R_S(\Omega)$	$C_{stray}(pF)$	rval
0.5	4.10×10^8	0.95	293	7.84	0.3126
0.05			1.75k	4.38	0.8369
0.005			13k	4.39	0.3854

2.2.3 Planar Electrode/Liquid Interface

The second experiment examined the impedance of the dual planar gold electrode / electrolyte interface. In this experiment, a droplet of solution ($\sim 20 \mu\text{L}$) was sandwiched between two gold electrodes, as shown in Figure 11. The wetted area on each electrode was controlled using an insulating O-ring (inner diameter ~ 0.23 cm, thickness ~ 0.16 cm) to define the contact line. The equivalent circuit for this configuration is identical to that in Figure 9b. Typical measured impedance spectra for this experiment (using $0.5\text{M Na}_2\text{SO}_4$), along with the fitted model are shown in Figure 12. The fitted parameters are: $\alpha = 0.89$, $K = 6.67 \times 10^5 \Omega (\frac{\text{rad}}{\text{s}})^\alpha$, $R_S = 29.8 \Omega$.

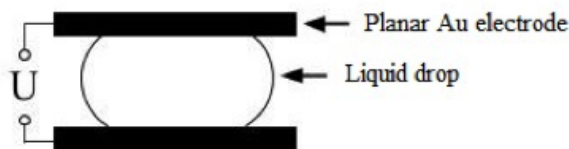


Figure 11: Experimental setup for testing planar electrode/liquid interface.

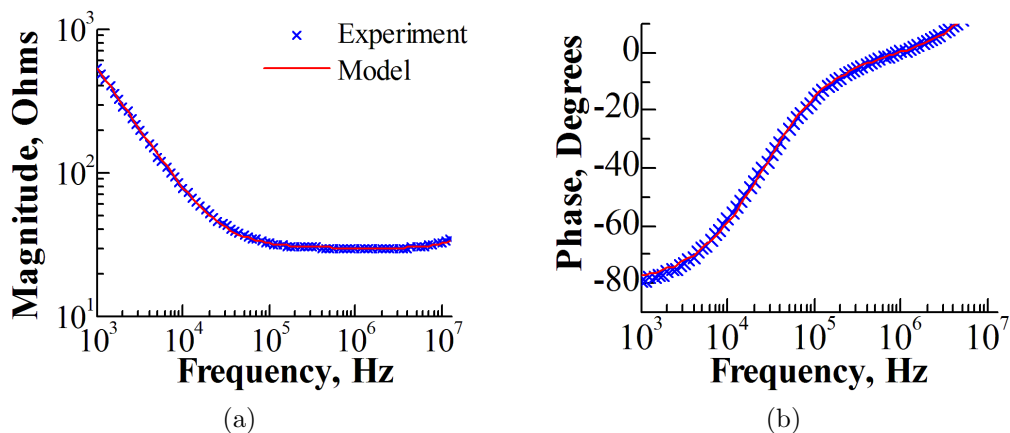


Figure 12: Experimental impedance and fitted model ($0.5\text{M Na}_2\text{SO}_4$).

The CPE power parameter α is different between the wire and the planar electrode configurations. The reason for this variation is not understood at this time. The parameter K in the model of the wire experiment is significantly larger than that

in the planar gold electrode test, which can be attributed with confidence to the significantly smaller wetted area of the wire/liquid interface in the wire test. Assuming a cylindrical shape for the drop (lower radius is 0.23 cm and height is 0.16 cm) and a 42.7 mS/cm conductivity for the 0.5M Na₂SO₄ solution [56], we can estimate the series resistance of the drop to be $R_S = \frac{1}{42.7 \text{ mS/cm}} \cdot \frac{0.16 \text{ cm}}{\pi 0.23^2 \text{ cm}^2} = 22.5 \Omega$. This is in fair agreement with the fitted value of 29.8 Ω .

2.2.4 Dielectric/Liquid Interface

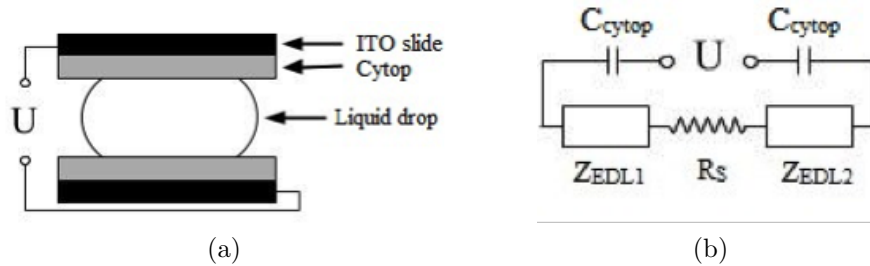


Figure 13: (a) Experimental setup; (b) equivalent circuit for the planar dielectric/liquid interface test.

The third experiment examined the planar dielectric/ liquid interface using the setup shown in Figure 13a, where a liquid drop is sandwiched between two parallel ITO electrodes, each covered with a Cytop film. (Since the ITO has a relatively large sheet resistivity (30-60 Ω /sq). Its impedance may not be negligible when considering the total impedance of the system. To solve this, the upper and lower plates were assembled so as to make the ITO resistance contribution constant in all of the experiments, regardless of changes in droplet position.) Measured impedance magnitude and phase spectra and the extracted reactance spectra are shown in Figure 14.

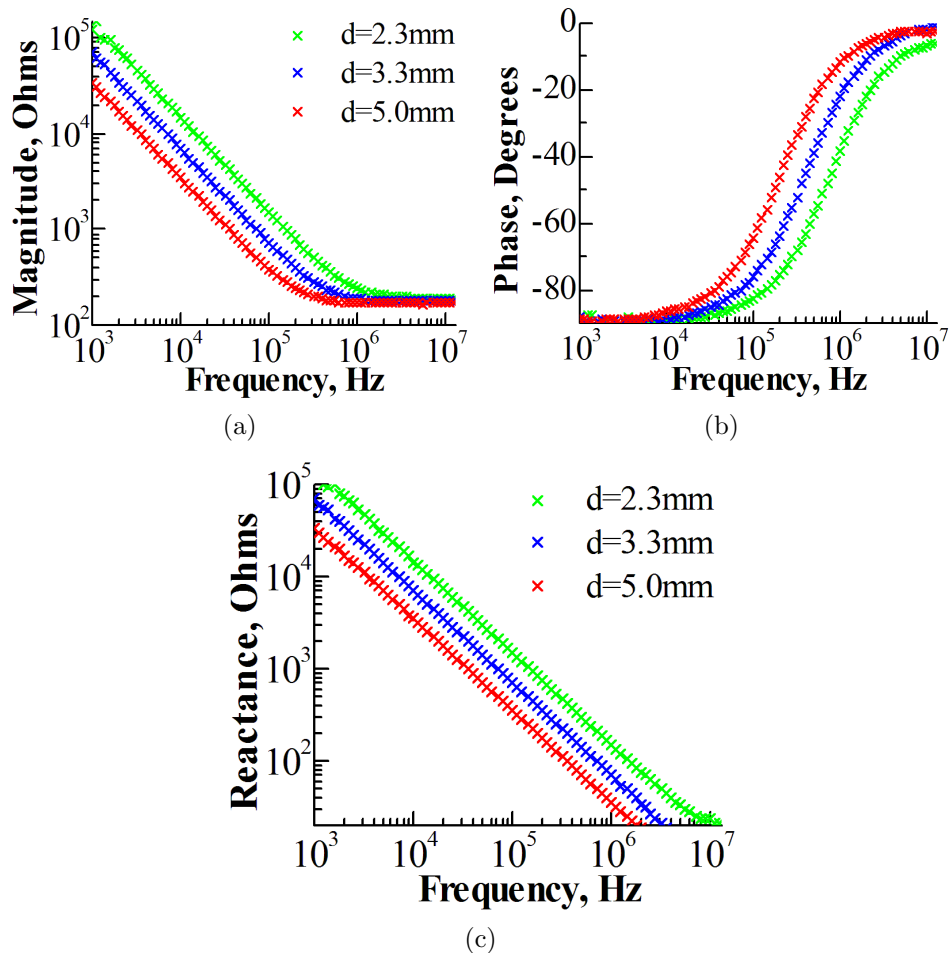


Figure 14: (a) Impedance magnitude and (b) phase spectra and (c) reactance spectra for Cytop coated ITO slides in contact with a 0.5M Na_2SO_4 liquid drop. Curves in various colors represent tests with different contact areas; "d" in the legend denotes the contact circle diameter.

The system has an equivalent circuit (Figure 13b) consisting of several lumped elements in series: the dielectric (Cytop) capacitance, the solution resistance, and elements characterizing the electrode double layers. Since the upper and lower contact diameters were confirmed to be identical via optical microscopy, the dielectric capacitance and double layer impedance of the upper and lower plates are taken to be the same. As discussed in the previous section, the double layer impedance is well

described with the CPE model. The total impedance can then be expressed as

$$\begin{aligned}
Z(\omega) &= R_S + 2Z_{cytop} + 2Z_{EDL} \\
&= R_S + 2\frac{1}{j\omega C_{cytop}} + 2K(j\omega)^{-\alpha} \\
&= R_S + \frac{2}{j2\pi f \frac{\epsilon_0 \epsilon_r \pi d^2}{4t_{cytop}}} + 2K(2\pi f)^{-\alpha} \exp[j(-\alpha \frac{\pi}{2})] \\
&= R_S + 2K(2\pi f)^{-\alpha} \cos(\alpha \frac{\pi}{2}) - j[\frac{4t_{cytop}}{\pi f} + 2K(2\pi f)^{-\alpha} \sin(\alpha \frac{\pi}{2})]
\end{aligned} \tag{5}$$

where d is the contact area diameter, and t_{cytop} is the Cytop layer thickness. The last line of this expression illustrates that both the resistive (real) and the reactive (imaginary) components of the impedance are not simple functions of frequency. However, as can be seen in Figure 14c, the experimental reactance spectra are linear in frequency, indicating first order RC behaviors. The double layer thickness is much smaller than the dielectric thickness (by at least an order of magnitude), so the impedance associated with the dielectric capacitance dominates that of the double layer (note that the area of both are the same). As a result, the total impedance is determined by the dielectric. The error when ignoring the double layer in this experiment is of the order of 0.01%.

Therefore, the third experimental setup can be well modeled without resort to any CPE terms, i.e.

$$Z(\omega) = R_S + 2\frac{1}{j\omega C_{cytop}} = R_S - j\frac{4t_{cytop}}{\pi f \epsilon_0 \epsilon_r \pi d^2} \tag{6}$$

Typical impedance spectra along with the fitted models are shown in Figure 15. The diameter d of the wetted area in this case was 2.3 mm, the Cytop thickness t_{cytop} was 29 nm, and the dielectric constant of Cytop ϵ_r was 2.1. Data from experiments with other wetted areas could also be modeled well with the RC model. The fitted series

resistance R_S is 193Ω . The only difference is that a proportionally scaled dielectric capacitance and bulk resistance must be used due to the difference in wetted areas.

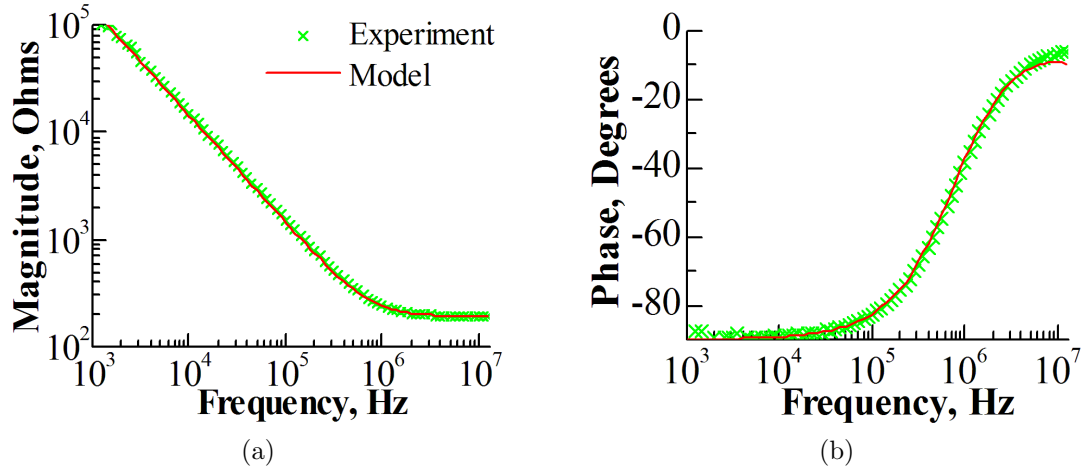


Figure 15: Typical impedance spectra and model impedance for Cytop coated ITO slides in contact with a 0.5M Na_2SO_4 liquid drop.

2.3 Impedance of Typical EWOD Arrangements and Implications for Area Determination

We first consider the total impedance of the three EWOD setups shown in Figure 8 with the goal of determining the dominant impedance (if any) in each case. Such an analysis indicates the degree to which the total impedance is dependent on the wetted area of the dielectric. The analysis, therefore, indicates to what extent impedance data can be used to identify wetted area.

2.3.1 EWOD with Wire Electrode

We now examine the impedance of a typical EWOD experiment, consisting of a sessile liquid droplet on a planar dielectric-coated electrode with a thin wire inserted into the droplet as the counter electrode, as shown in Figure 8a. The equivalent circuit of this configuration is a series combination of the EDL impedance at the wire/liquid interface, the bulk resistance of the droplet, and the dielectric capacitance at the liquid/ planar dielectric interface, therefore

$$Z(\omega) = K(j\omega)^{-\alpha} + R_S + \frac{1}{j\omega C_{dielectric}} \quad (7)$$

We now examine the relative magnitude of these terms. As the exponent α is close to 1 in all cases, the EDL impedance can be fairly well approximated as a parallel-plate capacitor with area A_{EDL} and thickness t_{EDL} . Thereby, Equation 7 can be approximated as

$$Z(\omega) = \frac{t_{EDL}}{j\omega\varepsilon_0\varepsilon_{r_EDL}A_{EDL}} + R_S + \frac{t_{dielectric}}{j\omega\varepsilon_0\varepsilon_{r_dielectric}A_{dielectric}} \quad (8)$$

The impedance ratio of two capacitances is then

$$\left| \frac{Z_{EDL}}{Z_{dielectric}} \right| = \frac{t_{EDL}}{t_{dielectric}} \cdot \frac{\varepsilon_{r_dielectric}}{\varepsilon_{r_EDL}} \cdot \frac{A_{dielectric}}{A_{EDL}} \quad (9)$$

In Equation 9, t_{EDL} is typically less than 1 nanometer for concentrated aqueous solutions [36], and $t_{dielectric}$ is generally tens to hundreds of nanometers in most thin-film EWOD systems. Thus, the order of magnitude of the first term $t_{EDL}/t_{dielectric}$ would be approximately $10^{-1} \sim 10^{-3}$. The second term, $\varepsilon_{r_dielectric}/\varepsilon_{r_EDL}$, is in the range of $10^{-1} \sim 1$, taking typical values of $\varepsilon_{r_dielectric}$ to be 2.1 (Cytop), 3.9 (Silicon dioxide), or 9.1 (Aluminum oxide) and ε_{r_EDL} to be 6 [36]. The liquid/dielectric interface area $A_{dielectric}$ is much larger than the thin wire/liquid interface area A_{EDL} , by a factor of $10^4 \sim 10^5$. Therefore, $|Z_{EDL}/Z_{dielectric}|$ will normally take a range from 1 to 10^4 . As a result, $|Z_{EDL}|$ is typically much larger than, or at least comparable to, $|Z_{dielectric}|$, taking a dominant role in the impedance spectrum. Therefore, to use the total impedance of the system as a measure of the wetted area of a sessile drop, the top wire must have a much larger area than typical (perhaps via high porosity) to compensate for the great disparity in thickness between the two capacitive elements. To more concretely support this conclusion, let us consider this setup with some typical numbers. Consider an aqueous sessile drop with a Cytop layer in an air ambient environment. Typically a sessile contact angle of 110° is exhibited. For a $10 \mu\text{L}$ -scale sessile droplet, the radius of the contact circle is approximately 2 mm. In thin-film electrowetting applications, the thickness of the dielectric layer ranges from tens to hundreds of nanometers. If we assume the Cytop thickness to be 50 nm to 500 nm, this will result in a dielectric capacitance of 4.67 to 0.467 nF. At 1 kHz, this dielectric capacitance yields an impedance magnitude of $3.4 \times 10^4 \Omega$ to $3.4 \times 10^5 \Omega$. The other important component that has a non-negligible contribution to

the total impedance is the EDL at the wire electrode/ electrolyte interface. Assuming one uses the same wire with a similar contact area as the experiments illustrated in Section 2.2.2, this EDL will contribute an impedance of $|Z_{EDL}| = |A(j\omega)^{-\alpha}| = |(4.10 \times 10^8)(j2\pi \cdot 1000)^{-0.95}|\Omega = 10^5\Omega$ at 1 kHz. Therefore, in this setup, the EDL component at the wire/ liquid interface dominates the total impedance. Given the fact that the EDL impedance changes with various applied bias [39], the total impedance spectra would not intuitively reflect the wetting behavior at the dielectric/ liquid interface.

2.3.2 EWOD with Planar Electrode

For EWOD setups with a parallel plate configuration as shown in Figure 8b, the equivalent circuit is a series combination of the EDL impedance at the upper plate interface, the bulk solution resistance, and the dielectric capacitance at the lower plate interface. This is similar to the scenario analyzed in Section 2.3.1; the only difference is that the EDL element here has an area comparable to the dielectric capacitor. The impedance ratio of the EDL capacitance and the dielectric capacitance can still be described with Equation 9. Since the areas are comparable in this case, both the second and third term on the right hand side of the equation have a numerical value close to one. Since the thickness ratio $t_{EDL}/t_{dielectric}$ typically has a value of $10^{-1} \sim 10^{-3}$, as discussed in Section 2.3.1, the dielectric capacitance will dominate the total impedance spectrum.

We now consider this setup with some typical numbers. If the upper plate is a planar gold electrode similar to that in Section 2.2.3, a good estimate of the impedance at 1kHz contributed by the EDL element at the upper interface with a contact area of about 0.16 cm^2 would be $|Z_{EDL}| = |A(j\omega)^{-\alpha}| = |(6.67 \times 10^5)(j2\pi \cdot 1000)^{-0.89}|\Omega = 278\Omega$. Still taking the 50-500 nm thick Cytop layer as the dielectric, a contact area of

0.16 cm² yields a dielectric capacitance of 5.9 - 0.59 nF, contributing an impedance that is $2.7 \times 10^4 - 2.7 \times 10^5 \Omega$ in magnitude at 1 kHz, which is 2 to 3 orders of magnitude larger than the EDL impedance at the same frequency. Therefore, in this setup, the dielectric capacitance dominates the total impedance, and the wetted area can be directly extracted from the impedance spectrum of the system.

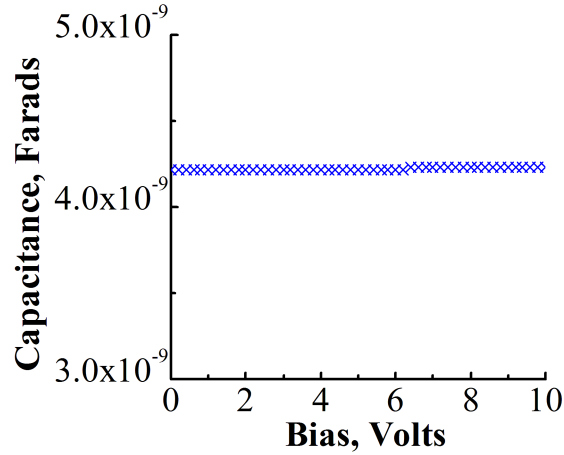
2.3.3 EWOD with Insulated Electrode

For EWOD setups using insulated electrodes on both sides, as shown in Figure 8c, the situation will be the same as that examined in Section 2.2.4. The EDL element at the dielectric/ liquid interface is negligible and the total impedance spectra is a reflection of the series combination of the dielectric capacitance at the upper and lower plates.

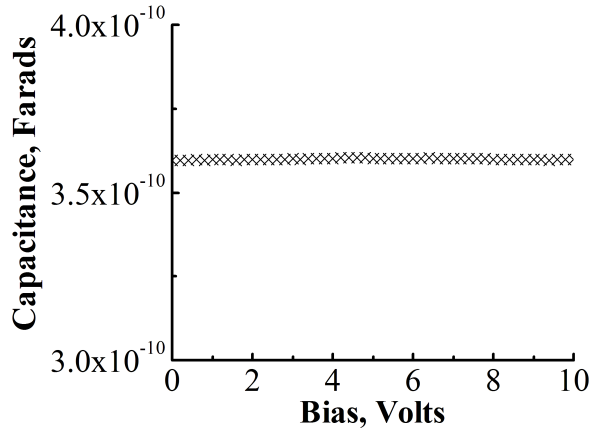
2.3.4 Invariance with Varying Bias

For the above models to be employed in determining droplet configuration in an EWOD system, the capacitance per unit area must be invariant to changes in the bias voltage applied. To demonstrate this, we measured the C-V characteristic of a EWOD setup with parallel planar electrodes. The bare electrode plate is an evaporated gold surface, while the other electrode is an aluminum layer, covered with an anodized aluminum oxide layer (43 nm) and a Cytop hydrophobic layer (17 nm). The aqueous electrolyte used is a 0.1 M Cs₂SO₄ solution. The change in cation from previous tests does not affect the results presented. The schematic of the setup is similar to that shown in Figure 8b, except that the liquid drops contact line is pinned on both plates by an insulating paint that defines circular regions. The contact area at the electrode/liquid and dielectric/liquid interface have diameters of ~ 0.37 cm and 0.28 cm respectively; their areas are fixed. During the experiment, the bare gold electrode

is grounded while the aluminum electrode is positively biased. Bias voltage is swept from 0 to 10 V, with a step of 0.2 V. A 10 mV sinusoidal perturbation voltage at 100 kHz is added to the bias for determining the impedance. A similar experiment was carried out with the same setup, the only difference is that the dielectric used was a thick Cytop hydrophobic layer (~ 457 nm). Measured C-V results are shown in Figure 16 for both experiments.



(a)



(b)

Figure 16: Measured C-V result for a parallel plate EWOD setup with the droplet pinned on both sides with the dielectric being: (a) a bilayer composed of a 43 nm aluminum oxide layer topped by a 17 nm Cytop hydrophobic layer; (b) a single 457 nm Cytop layer.

As can be seen from the figure, the measured capacitance remained constant with varying bias in each experiment. As the contact area at the electrode/ electrolyte interface is larger than that of the dielectric/ electrolyte interface, with the analysis in the previous section, one may predict that the measured capacitance is a direct reflection of the dielectric capacitance. Using the dielectric permittivity, thickness, and the contact diameter, the dielectric capacitance of the Al₂O₃ Cytop bilayer was estimated to be 4.23 nF, which closely matches the measured value. Therefore, the capacitance of the system is a direct measure of the contact area at the dielectric surface, and, since the wetted area is held fixed in the experiment, the capacitance per unit area is invariant to the bias voltage used.

2.4 Conclusion

The electrical properties of several experimental EWOD configurations were analyzed using impedance spectroscopy. Models were developed and validated using experimental data. The wire electrode/ liquid interface and planar electrode/ liquid interface exhibit electric double layer behaviors which can be well characterized using a constant phase element (CPE) model. The planar dielectric/ liquid interface comprises a series combination of the dielectric capacitances and the electric double layers, yet exhibits first order RC behavior overall since the dielectric capacitance dominates that of the CPE in the impedance spectra.

Three typical electrowetting setups were examined. For (a) a conventional setup with an inserted wire, the EDL at the wire electrode dominates the impedance spectrum. For (b) a parallel plate setup, with one plate being a bare electrode and the other covered with a dielectric, the impedance of the EDL element at the bare electrode plate is much smaller in comparison to the dielectric capacitance. For (c) a parallel plate setup with two dielectric covered electrodes, the impedance is dominated by the series combination of these dielectric capacitances and the EDL can be ignored. Therefore, in order to interrogate drop configuration via impedance spectroscopy, EWOD setups need to be properly designed so that the dielectric capacitance dominates the total impedance spectrum of the system. This can be achieved for either parallel plate setups we have described. The inserted wire setup can only be used if the surface area of the wire is greatly enhanced.

3 Interrogation of Droplet Configuration

3.1 Introduction

With the analysis in Chapter 2, we concluded that wetted area could be directly extracted from the impedance spectra of the system when the setup of the EWOD system ensures that the capacitance of the dielectrics wetted area dominates the total impedance spectrum. With the wetted area known, various parameters regarding the configuration of a microliter aqueous droplet, including contact angle, liquid/ ambient interfacial tension, and volume, can be accurately determined by solving for the capillary shape of the drop. This being a well-posed mathematical problem, it could be solved quickly and precisely with a well-developed computer program. Therefore, it has the potential to expand the application of the electrical characterization method to more and different EWOD setups.

3.2 Experiments

3.2.1 Approaches

The device under test consists of a droplet of conducting liquid spanning between two parallel plate electrodes and forming a capillary bridge, as shown in Figure 17. The bridge contact line is pinned on the lower plate (referred to as the passive surface) and electrowets on the upper plate (referred to as the active surface) when a voltage bias is applied between the two electrodes. A dielectric layer is present on the active surface electrode while the passive surface electrode is uncovered.

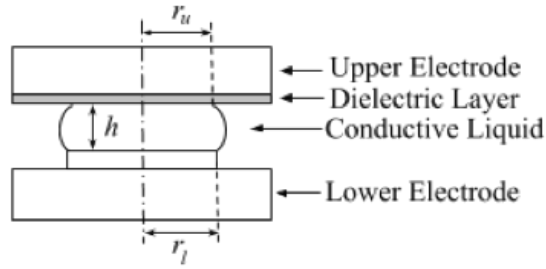


Figure 17: Experimental setup: Parallel plate configuration with the liquid bridge pinned on lower surface and electrowetting on upper surface.

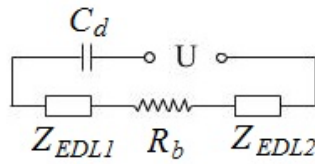


Figure 18: Electrical impedance model of experimental setup.

An electrical impedance model of the device, shown in Figure 18, consists of four elements in series: (1) the capacitance of the wetted area of the dielectric layer on the active surface, C_d ; (2) the resistance of the liquid bridge, R_b ; and (3&4) the impedance of the electrical double layers at the liquid/solid interfaces, Z_{EDL1} and Z_{EDL2} . This approach to interrogating droplet configuration relies upon the impedance of the electrical double layers being much smaller than that of the dielectric layer. In this case, the measured capacitance of the circuit will be that of the dielectric layer. In this chapter, we demonstrate the efficacy of two approaches for interrogating droplet configuration using electrical impedance measurements, including the determination of contact angle during electrowetting:

Approach I (Problem I): If θ_0 and σ are unknown, the contact angle may be determined without using Equation (1), provided the thickness and permittivity of the dielectric as well as the liquid bridge volume and height are known. Since the wetted area A is directly proportional to the measured capacitance, the contact radii may be

determined. Given the boundary condition on the passive surface, the droplet volume, and bridge height, the contact angle on the active surface may be found using the wetted area by exploiting Plateau's solutions for the shape of an axisymmetric capillary bridge [40, 41].

Approach II (Problems II, III, and IV): With capacitance measurements at several voltage values, Equation (1) may be employed together along with Plateau's solution to determine the contact angles at each voltage, droplet volume, and the interfacial tension of the liquid/ambient fluid interface. Only the permittivity and thickness of the dielectric layer are needed to carry out this identification.

3.2.2 Materials and Fabrication

In the experiment, the lower (passive) surface was a planar gold electrode fabricated by electron beam physical vapor deposition (EBPVD) on a silicon wafer. Insulating electrical tape (Vinyl Tape, VWR) with a punched circular hole (radius = 0.165 cm) was placed on this surface to pin the lower contact line. The diameter of the hole was measured with an optical microscope. The upper plate, serving as the active surface, is an indium tin oxide (ITO) electrode ($\text{SnO}_2:\text{In}_2\text{O}_3$, Sigma-Aldrich, 30-60 Ω/sq , 300-600 \AA) covered by a 400-500 nm thick hydrophobic fluoropolymer dielectric layer. To fabricate this film, two layers of 5wt% Cyttop (CTL-809M, Solvent CT-Solv.180, Asahi Glass) were spin-coated on the ITO electrode. A low-temperature half-dry (90°C, 15 minutes) is performed after spinning the first layer. A final high-temperature annealing at 160°C follows the second spinning to enhance layer adhesion to the substrate. The conducting liquid used was a 0.1M sodium sulfate aqueous solution. All tests were carried out in a surrounding insulating silicone oil environment. The oil used was a mixture of Dow Corning OS-10, OS-20, and OS-30 (1:8:1 by weight). [42] Because of the ambient oil environment, losses of the bridge solution

due to evaporation during testing were negligible. The surface energy of the oil/water interface was experimentally determined via a tensiometer to be 16.9 mN/m. The gap between plates was set using spacers cut from silicon wafers. To prevent a potential leakage path between the upper and lower electrodes, the spacers that support the upper plate were placed on the test stage instead of directly on the lower plate.

3.2.3 Electrowetting and Impedance Spectroscopy

Electrowetting test and synchronous C-V characterization were performed using the HP 4192A Impedance Analyzer. The DC bias for electrowetting on the active surface was applied with the internal bias supply of the analyzer. The bias was increased during a test with steps of 0.2 V by a LabView program that recorded the impedance measurement. The impedance analyzer was operated in average mode, where the output at each bias was the average of seven measurements. The test signal was a sinusoidal signal provided by the analyzers internal frequency synthesizer, the frequency and signal level of which are 100 kHz and 50 mVrms, respectively.

3.2.4 Dominance of Dielectric Layers Impedance

As demonstrated in the previous chapter, the electric double layer (EDL) impedance at the metal/ electrolyte interface can be well described with the constant phase element (CPE): $Z_{EDL}(\omega) = A(j\omega)^{-\alpha}$. Previous experiments have shown that the typical value of α for 0.5M Na₂SO₄ solution/ flat gold interface is 0.89. The other parameter A , however, varies with different contact area and ranges from 10^5 to $10^8 \Omega(\frac{rad}{s})^\alpha$ for typical contact area values of about 10^{-6} to 10^{-1} cm^2 in our experiments.

A brief calculation is reviewed here that indicates the validity of the hypothesis of dielectric layer dominance for the experiment. Model parameters were assigned typical numeric values. For the CPE at the lower plate interface, the contact area

is 0.086 cm^2 calculated from the hole radius of 0.165 cm . Therefore, assuming $A = 10^5 \Omega (\frac{\text{rad}}{\text{s}})^\alpha$ and taking α to be 0.89 , the EDL magnitude at 100 kHz is calculated to be

$$Z_{EDL} = A(j2\pi f)^{-\alpha} = 0.69\Omega \quad (10)$$

For the dielectric capacitance at the top plate, assuming a dielectric thickness $t_{cytop}=457 \text{ nm}$ and contact circle radius $r_u=0.165 \text{ cm}$, the dielectric capacitance is

$$C_{dielectric} = \frac{\varepsilon_0 \varepsilon_d \pi r^2}{t_{cytop}} = 348 \text{ pF} \quad (11)$$

Corresponding impedance magnitude contributed by the dielectric layer at 100 kHz is then calculated to be

$$|Z_{dielectric}| = \left| \frac{1}{2\pi f C_{dielectric}} \right| = 4570\Omega \quad (12)$$

It is clear that the magnitude of the EDL impedance Z_{EDL} is only 0.015% of that of the dielectric impedance $Z_{dielectric}$, and therefore is negligible in the series equivalent circuit. As a result, the capacitance of the dielectric can be assumed to be equivalent to the measured capacitance.

The key factor in achieving this dominance property is the ratio of the wetted dielectric area to the wetted passive electrode area. If this ratio is high, the impedance of the electrical double layer will dominate the total impedance spectrum and it will be difficult to determine the wetted active surface area from the collected data. To be more specific, since we are using the existing electrical contacts to perform the measurement, the measured impedance will always be the total impedance of the system. Therefore, to use the electrical measurement to characterize EWOD, one needs to make sure that the wetted area can be correctly extracted from the

measured impedance data. For example, Verheijen and Prins [26] measured the C-V characteristic of the most commonly seen EWOD setup containing a sessile drop resting on a flat dielectric-covered electrode with a metal probe as the counter electrode. They then calculated the contact area directly from the capacitance data using known dielectric properties. If the dielectric layer in the setup is now switched to a much thinner one (from $\sim 10 \mu\text{m}$ to $\sim 30 \text{ nm}$), their method would not work since the dielectric capacitance is much larger and the total capacitance will be dominated by the double layer element at the probe/liquid interface. A detailed analysis on the electrical models of various elements appeared in EWOD setups and related typical parameter values can be found Chapter 2.

3.3 Results and Discussion

3.3.1 Capacitance-Voltage Results

The measured C-V result is shown in Figure 19a. During the measurement, the active surface electrode is always held at higher potential than the passive surface electrode. Upon the application of an increasing bias, the bridge electrowets the active surface, increasing the contact area and therefore the measured capacitance. Using the known dielectric thickness (457 nm) and permittivity ($\epsilon_r = 2.1$ for Cytop), the corresponding wetted area radius was calculated by

$$r_u = \sqrt{\frac{C_d t_d}{\epsilon_0 \epsilon_d \pi}} \quad (13)$$

and is shown in Figure 19b. The wetted area determined from this measurement is the same as that obtained from direct optical measurements of the droplet diameter.

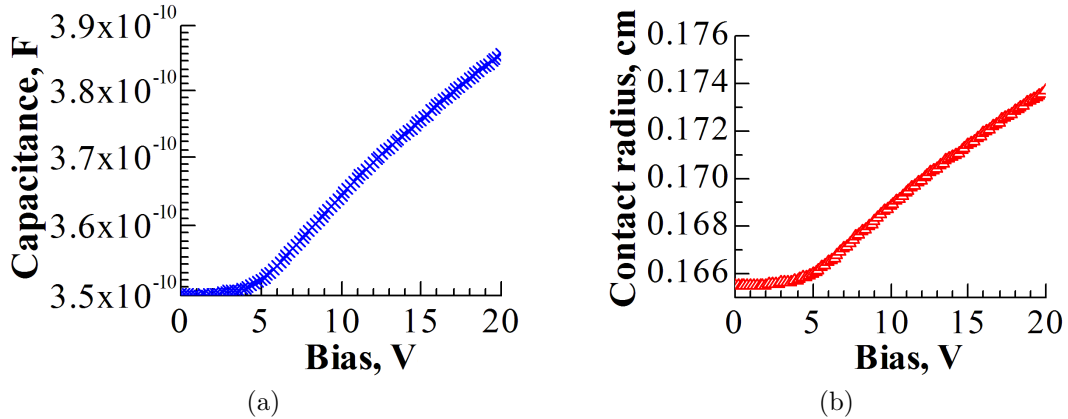


Figure 19: (a) Measured C-V result and (b) calculated radius of wetted area (r_u).

3.3.2 Modeling Theory and Method

We first introduce two conditions that are critical for the modeling of the bridge shape. First, note that the capillary length h_c , defined as $h_c = \sqrt{\frac{\sigma}{\Delta\rho g}}$, is 0.281 cm for

our experiment. Here $\Delta\rho$ denotes the density difference between liquid and oil and g denotes the gravitational acceleration. Since the capillary length is much larger than half of the bridge height 0.022 cm, gravitational forces is insignificant in comparison to the surface tension and may be neglected in finding the bridge shape. [43] Second, as the experiment was carried out in oil ambient, evaporation loss of the bridge is nonexistent.

Under these conditions, the profile of the axisymmetric capillary bridge between two parallel plates may be categorized by the Plateau sequence of shapes. [44] With the introduction of the non-dimensional capillary pressure p , the Plateau sequence of shapes is classified into nodoid ($p < 0$, $p > 1$), unduloid ($0 < p < 0.5$, $0.5 < p < 1$), and special cases of catenoid ($p = 0$), cylinder ($p = 0.5$), and sphere ($p = 1$). To explain the modeling approach in greater detail, we first introduce several definitions. Let ρ denote the non-dimensional profile radius and ζ denote the non-dimensional axial coordinate. Define the non-dimensional radii ρ_0 and ρ_1 in terms of the non-dimensional pressure p via: $\rho_0 = |p|$ and $\rho_1 = |1 - p|$. Finally, let $v(\rho)$ denote the non-dimensional bridge volume, $\zeta(\rho)$ denote the non-dimensional axial coordinate, θ denote the contact angle, and κ denote the scale factor that connects the corresponding non-dimensional and physical parameters. Then the upper and lower contact radii, axial coordinate, and bridge volume can be expressed as: $r_u = \kappa\rho_u$, $r_l = \kappa\rho_l$, $z = \kappa\rho$, $V_n = \kappa^3\rho$. The analytical expressions characterizing the Plateau sequence of shapes are summarized in Table 2. Note that all of these coordinate, angle, and volume functions are implicit functions of p .

Table 2: Analytical expression of the Plateau sequence.

	Bridges with “neck”				Bridges with “haunch”		
	$p < 0$	$p = 0$	$0 < p < 0.5$	$p = 0.5$	$0.5 < p < 1$	$p = 1$	$p > 1$
	Nodoid $\chi = -1$	Catenoid	Unduloid $\chi = +1$	Cylinder	Unduloid $\chi = +1$	Sphere	Nodoid $\chi = -1$
Notation	$q_1 = \sqrt{1 - \rho_0^2/\rho_1^2}$ $\phi_1 = \arcsin(q_1^{-1}\sqrt{\rho_0^2/\rho^2})$			/	$q_2 = \sqrt{1 - \rho_1^2/\rho_0^2}$ $\phi_2 = \arcsin(q_2^{-1}\sqrt{\rho^2/\rho_0^2})$		
Shape	$\zeta(\rho) = \rho_1 E(\phi_1, q_1) + \chi \rho_0 F(\phi_1, q_1)$ $-\rho^{-1}\sqrt{(\rho^2 - \rho_0^2)(\rho_0^2 - \rho^2)}$			$\rho = \rho_0$	$\zeta(\rho) = \rho_0 E(\phi_2, q_2)$ $+(1 - \rho_0)F(\phi_2, q_2)$		
Slope	$\tan \theta = d\zeta/d\rho$ $\cos^2 \theta = (\rho^2 - \rho_0^2)(\rho_1^2 - \rho^2)/\rho^2$						
Volume	$v(\rho) = 2 \int_{\rho_0}^{\rho} \pi \tilde{\rho} \zeta(\tilde{\rho}) d\tilde{\rho}$ $= \frac{2}{3} \pi \rho_1 \beta E(\phi_1, q_1) - \rho_0^2 F(\phi_1, q_1)$ $-(\beta^2 + \rho^2)\sqrt{(\rho^2 - \rho_0^2)(\rho_1^2 - \rho^2)}$ $/(\rho_0 \rho_1) $ $\beta = 2\rho_0^2 + 2\rho_1^2 + 3\chi\rho_0\rho_1$			$\pi\rho_0^2\zeta(p)$	$v(\rho) = 2 \int_{\rho_0}^{\rho} \pi \tilde{\rho} \zeta(\tilde{\rho}) d\tilde{\rho}$ $= \frac{2}{3} \pi \beta \rho_0 E(\phi_2, q_2) - \rho_0 \rho_1^2 F(\phi_2, q_2)$ $+ \rho \sqrt{(\rho^2 - \rho_1^2)(\rho_0^2 - \rho^2)} $ $\beta = 2\rho_0^2 + 2\rho_1^2 + 3\chi\rho_0\rho_1$		

Each capillary bridge profile must fall within one of three cases:

- Case 1: Bridge with neck or haunch;
- Case 2: Bridge without neck that satisfies $\rho_1 > \rho_u > \rho_l > \rho_0$, or bridge without haunch that satisfies $\rho_0 > \rho_l > \rho_u > \rho_1$;
- Case 3: Bridge without neck that satisfies $\rho_1 > \rho_l > \rho_u > \rho_0$, or bridge without haunch that satisfies $\rho_0 > \rho_u > \rho_l > \rho_1$.

Illustrative profiles (unduloid shape) can be found in Table 3.

Table 3: Illustrative profiles for axisymmetric bridges with unequal contact angles.

	Case 1	Case 2	Case 3
$\rho_0 < \rho_1$			
$\rho_0 > \rho_1$			

Analytical expressions characterizing the more general bridge height and volume for these bridges are:

For Case 1:

$$\begin{cases} \zeta_1 = \zeta(\rho_u, p) + \zeta(\rho_l, p) \\ v_1 = \frac{1}{2}[v(\rho_u, p) + v(\rho_l, p)] \end{cases} \quad (14)$$

For Case 2:

$$\begin{cases} \zeta_2 = \zeta(\rho_l, p) - \zeta(\rho_u, p) \\ v_2 = \frac{1}{2}[v(\rho_l, p) - v(\rho_u, p)] \end{cases} \quad (15)$$

For Case 3:

$$\begin{cases} \zeta_3 = \zeta(\rho_u, p) - \zeta(\rho_l, p) \\ v_3 = \frac{1}{2}[v(\rho_u, p) - v(\rho_l, p)] \end{cases} \quad (16)$$

3.3.3 Problem I: Find the Contact Angle

With the measured C-V data and calculated contact radius (Figure 19), our first problem is to find the contact angle change as a function of applied bias voltage. In other words, the mathematical problem to be solved in Problem I is: *Given bridge volume V , height h , upper and lower wetted area radii r_u and r_l , find the bridge shape and the upper surface contact angle.*

To solve for this problem, we must first assume which of the three bridge-profile cases applies. Denoting the case by integer i ($i = 1, 2, 3$), the solution may then be determined by solving the following two-dimensional root finding problem:

$$\begin{cases} h = \kappa \zeta_i(\rho_u, \rho_l, p) = \kappa \zeta_i(\frac{1}{\kappa} r_u, \frac{1}{\kappa} r_l, p) \\ V = \kappa^3 v_i(\rho_u, \rho_l, p) = \kappa^3 v_i(\frac{1}{\kappa} r_u, \frac{1}{\kappa} r_l, p) \end{cases} \quad (17)$$

where h , V , r_u , r_l are the known values and p , κ are the unknown variables. Once p and κ are found, the bridge shape is uniquely determined. The contact angle at the active surface can then be determined by calculating the profile slope at the three-phase contact line. If the wrong case is assumed, one would not be able to find a solution to Equation (17).

Using the droplet volume (4.2 μL), droplet height (0.044 cm), lower contact line radius (0.165 cm), and the calculated contact line radius for the active surface (shown in Figure 19b), the root finding problem was solved for each bias voltage value using a Mathematica program. The computed contact angles are plotted in Figure 20 as a function of the applied bias voltage. The electrowetting behavior predicted by the LY equation is also included. For calculating the LY curve, experimentally obtained values of surface tension and dielectric properties were used. The calculated values of contact angle found via Approach I closely match those obtained from the LY

relationship. In our experiment, the gap between electrodes is in the μm range. In addition, the setup is placed in an acrylic container filled with oil, which makes the contrast between the liquid drop and ambient environment extremely poor. Therefore, it is extremely difficult to determine the contact angle using conventional side-view imaging. However, the contact circle diameter at the active surface (top ITO plate) has been optically confirmed with top-view imaging. Since the relationship between the contact area and the wetting angle is known, this correspondence validates the utility of using electrical interrogation to determine the contact angle as a function of voltage.

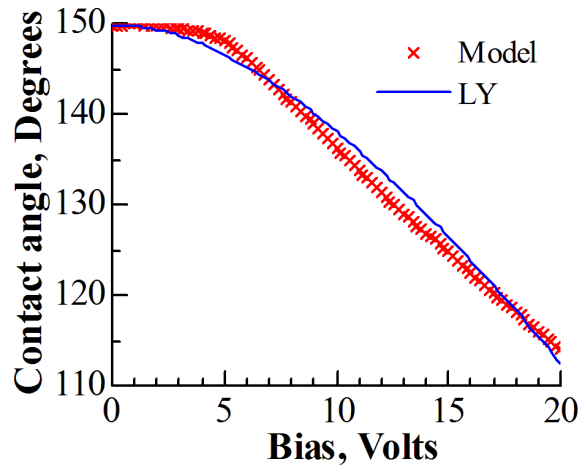


Figure 20: Contact angle calculated by Approach I as a function of bias voltage. Also shown is LY curve determined from oil/ electrolyte surface tension and layer dielectric properties.

3.3.4 Problem II: Find the Surface Tension

The second problem we will solve is to determine the electrolyte/oil interface tension from the impedance measurement results. The mathematical description for this problem is: *Given bridge volume V , height h , upper and lower wetted area radii r_u and r_l , find the liquid/ambient interfacial tension.*

As is shown in the previous section, provided the dielectric thickness and per-

mittivity, the contact radius at the active surface can be found from the capacitance results via Equation (13). In this problem, denote the Plateaus solution at each applied voltage U_j as (p_j, κ_j) , where $j=0,1,2,,N$. By solving (17) at voltage U_j for (p_j, κ_j) , the contact angle at the active surface θ_{uj} can be found in the same manner as in Problem I.

$$\begin{cases} h = \kappa_j \zeta_i(\frac{1}{\kappa_j} r_{uj}, \frac{1}{\kappa_j} r_{lj}, p_j) \\ V = \kappa_j^3 v_i(\frac{1}{\kappa_j} r_{uj}, \frac{1}{\kappa_j} r_{lj}, p_j) \end{cases} \quad (18)$$

As the angle changes with voltage as dictated by the LY relationship, surface tension σ_j can then be found by solving the LY equation at each voltage U_j . The derived explicit expression is

$$\sigma_j = \frac{\varepsilon_0 \varepsilon_d}{2t_d(\cos\theta_{uj} - \cos\theta_{u0})} U_j^2 \quad (19)$$

With multiple capacitance measurements performed at different voltages U_j , the value of σ can be found for each measurement, and a final estimate can be obtained by averaging these values. Using the capacitance results in Figure 19, the calculated surface tension was found at each voltage and is plotted in Figure 21. Also shown in the figure is the $\sigma=16.9$ mN/m measured with a tensiometer. A tensiometer is an instrument used to measure the surface tension at an air-liquid or liquid-liquid interface. The type of tensiometer we used is a Willhelmy plate, where a plate orients perpendicular to the interface and the force exerted on it due to wetting is measured [45].

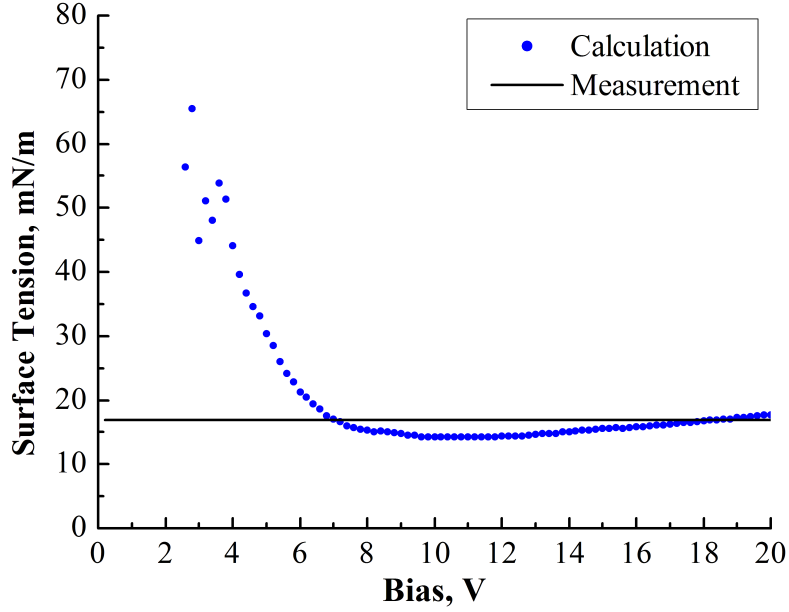


Figure 21: Liquid/ambient interfacial tension σ calculated by Approach II as a function of bias voltage.

At low voltages (approximately below 6 V), there is a large variation in the estimates of surface tension. This is because there has been little change in θ_{uj} from the zero voltage value θ_{u0} due to contact angle hysteresis yielding a pinned contact line. Contact angle hysteresis is defined as the difference between the advancing (maximal) angle and receding (minimal) angle, and can be experimentally observed as that the static contact angle at a given location can be made to vary within certain limits without causing perceptible movement of the contact line [46]. Averaging the values of σ from 6 V to 20 V, where the data influenced more by contact angle hysteresis are eliminated and the estimates are much more consistent, we find a final estimate of σ to be 16.3 mN/m, which is less than 4% lower than the value obtained with a tensiometer.

3.3.5 Problem III: Find the Drop Volume

As mentioned in the introduction, determining the liquid droplet volume is often of great importance in many EWOD related microfluidic applications. We will demonstrate in this section that the droplet volume can be found with a high accuracy by utilizing the impedance measurement results. The mathematical problem to be solved is: *Given the liquid bridge height h , contact angle at the active surface θ_u , upper and lower wetted radii r_u and r_l , find the bridge volume V .*

For solution of this problem we will assume that the bridge height is known as this is common in microfluidic devices. By applying a voltage U_j and performing a capacitance measurement at this voltage, the wetted area or radius r_{uj} at the active surface can be found, if the dielectric layer properties are known. Then, with the contact angle at the active surface θ_{uj} , the dimensionless pressure p_j and the scale factor κ_j can be found by solving the following two-dimensional root-finding problem:

$$\begin{cases} h = \kappa_j \zeta_i(\frac{1}{\kappa_j} r_{uj}, \frac{1}{\kappa_j} r_{lj}, p_j) \\ \cos^2 \theta_{uj} = \frac{(\rho_{uj}^2 - \rho_0^2)(\rho_1^2 - \rho_{uj}^2)}{\rho_{uj}^2} \end{cases} \quad (20)$$

where $\rho_{uj} = \frac{1}{\kappa_j} r_{uj}$, $\rho_0 = |p|$, and $\rho_1 = |1 - p|$. The droplet volume can then be calculated via $V = \kappa_j^3 v_i(\frac{1}{\kappa_j} r_{uj}, \frac{1}{\kappa_j} r_{lj}, p_j)$. In addition, if one is sufficiently familiar with the system so that the initial contact angle θ_0 is known and that the applied voltage does not exceed the saturation voltage, an estimate of the contact angle θ_{uj} can be found via the LY equation and the angle measurement can therefore be omitted.

With contact angle predicted by the LY equation and the C-V results shown in Figure 19, the droplet volume is calculated at each voltage U_j ($j \neq 0$) and plotted in Figure 22. The initial contact angle is taken to be 150° . A final estimation of the

droplet volume by averaging these volume values at different voltages is calculated to be $4.21 \mu\text{L}$. And the standard deviation of these values is calculated to be $0.01\mu\text{L}$. The final estimate diverges from the experimental value specified by the pipette dispenser by about 0.2%, which is smaller than the accuracy of the dispenser.

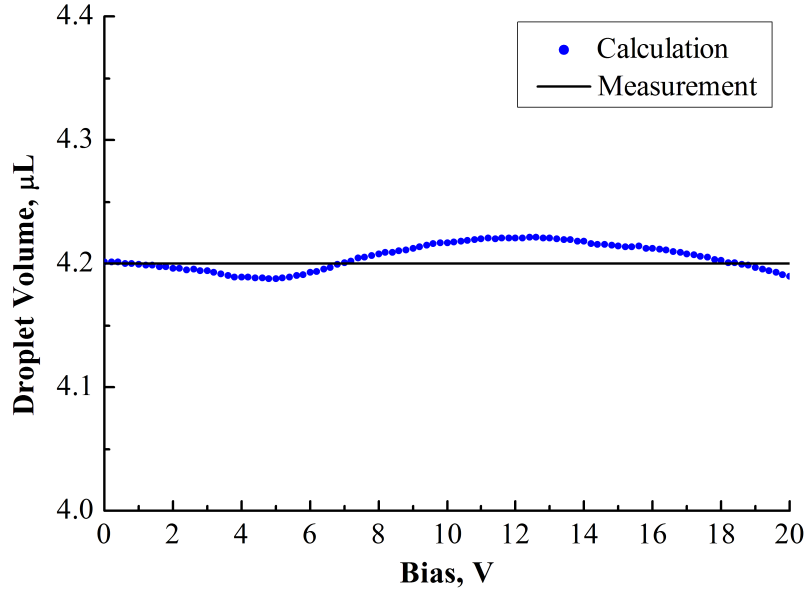


Figure 22: Droplet volume calculated by Approach III as a function of bias voltage. Also shown is the experimental drop volume ($4.20 \mu\text{L}$) specified by the pipette dispenser.

3.3.6 Problem IV

In Problem III, the initial zero bias contact angle θ_0 and the liquid/ambient surface tension σ are known and used for calculating the upper contact angle θ_{u_j} in (19). However, if one or both of these two parameters are unknown, they may still be found by the following approach.

Let us start our analysis with the simpler case where σ is known and θ_0 is unknown. Specify a set of possible θ_0 values $\theta_{0,k}$ ($k=1,2,3,N$). Then with each hypothetical

value $\theta_{0,k}$, the angle at each voltage U_j can be found with the LY equation. Following an algorithm similar to Approach III, drop volume $V_{k,j}$ at each voltage can then be calculated. For each hypothetical $\theta_{0,k}$, the variance of volume data $V_{k,j}$ can be calculated and is denoted S_k . Then the index k that corresponds to the minimum value of S_k can be found and denoted k_{min} . Then, the solution to this problem is chosen as the corresponding value of initial contact angle, $\theta_0 = \theta_{0,k_{min}}$, and the average of the computed values, $V = \frac{1}{N} \sum_j V_{(k_{min},j)}$. This technique is now applied to the data in Figure 19. The range of the hypothetical θ_0 values was $140^\circ \sim 160^\circ$; set values were specified with an increment of 1° . The standard deviation S_k of the calculated drop volume as a function of the initial angle $\theta_{0,k}$ is shown in Figure 23. The minimum S_k value was achieved at $\theta_0 = 153^\circ$, and the corresponding average drop volume is $4.23 \mu\text{L}$. The difference compared to the experimental values are 2% and 0.7% respectively.

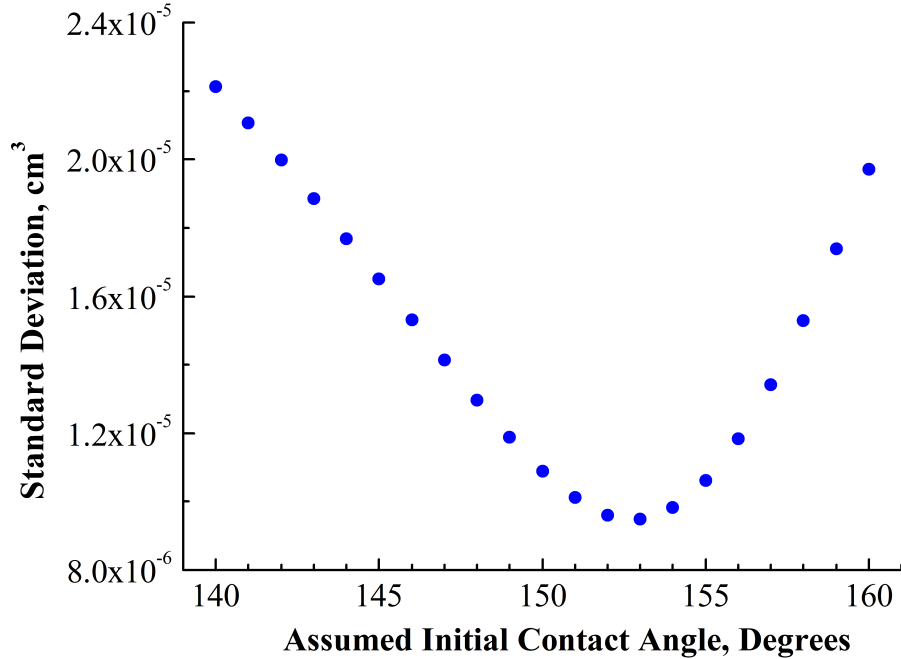


Figure 23: Standard deviation of calculated drop volume as a function of the assumed initial contact angle.

For the more difficult problem where both θ_0 and σ are unknown, a similar algorithm can be used where hypothetical values of σ are also postulated and an additional loop of calculation is employed. The set of data that has the minimum variance then gives the best estimates of θ_0 and σ . This analysis technique was applied to the capacitance data presented in Figure 19. Figure 24 shows the standard deviation in the calculated volume as a function of assumed values of θ_0 and σ . The minimum variance yields the estimates $\theta_0 = 165^\circ$, $\sigma=26.5$ mN/m, and $V=4.35$ μL . These estimates may be compared to the actual values $\theta_0 = 150^\circ$, $\sigma=16.9$ mN/m, and $V=4.20$ μL . As can be seen in Figure 24, there is a long and narrow region in the parameter space where the variance is essentially the same as the minimum value. This makes it difficult to determine the estimates accurately, as this algorithm intrinsically has a very high requirement on the accuracy of the EWOD experimental data and the few known physical parameters that are used in the calculation. There exist areas within the parameter space that exhibit low error sensitivity, that is, the calculated values are not highly sensitive to errors in the parameters.

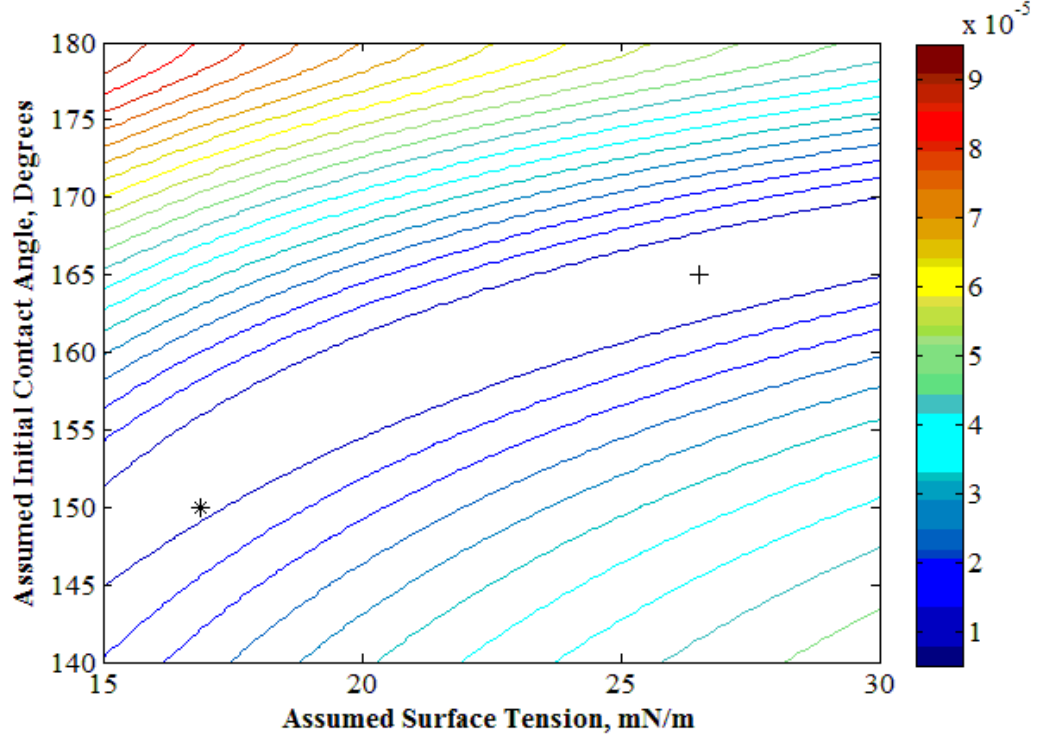


Figure 24: Standard deviation of calculated drop volume as a function of the assumed initial contact angle and surface tension. The calculated minimum point (26.5, 165) and the true parameter values (16.9, 150) are also shown.

A simple simulation verifies this explanation of the estimate errors seen. Assume an ideal EWOD system like that in Figure 17, in which the contact angle on the active surface θ_u ideally follows the LY relation (e.g., no hysteresis). Provided surface tension σ , initial angle θ_0 , drop volume V , and bridge height h , the ideal C-V (equivalently, r_u - V) relation can be found by solving the following three-dimensional root-finding problem for p , κ , and r_u :

$$\begin{cases} \cos^2 \theta_{uj} = \frac{(\rho_{uj}^2 - \rho_0^2)(\rho_1^2 - \rho_{uj}^2)}{\rho_{uj}^2} \\ V = \kappa_j^3 v_i \left(\frac{1}{\kappa_j} r_{uj}, \frac{1}{\kappa_j} r_{lj}, p_j \right) \\ h = \kappa_j \zeta_i \left(\frac{1}{\kappa_j} r_{uj}, \frac{1}{\kappa_j} r_{lj}, p_j \right) \end{cases} \quad (21)$$

Using the ideal C-V result as the input data, the same calculation as previously can be carried out. The computed standard deviation of volume as a function of the assumed initial angle value and assumed surface tension value is shown in Figure 25. As can be seen, the shallow region of the volume standard deviation is a significantly smaller region than in Figure 24, indicating that the effectiveness of this method for simultaneously identifying multiple droplet parameters is indeed highly dependent on the accuracy of the measurements and the validity of Lippmann-Young. Not surprisingly, the minimum deviation is obtained with the parameter values used in generating the simulated data. We think that trying to simultaneously identify multiple parameters is a relatively ambitious goal. The Laplace equation or Plateau sequence of shapes is a very accurate model that is physically meaningful. Any modeling using this method should have a high requirement on the accuracy of the input parameters. We have shown in this chapter that identifying a single parameter can be well achieved with our measured data and identifying two results in an area of low error sensitivity in the parameter space.

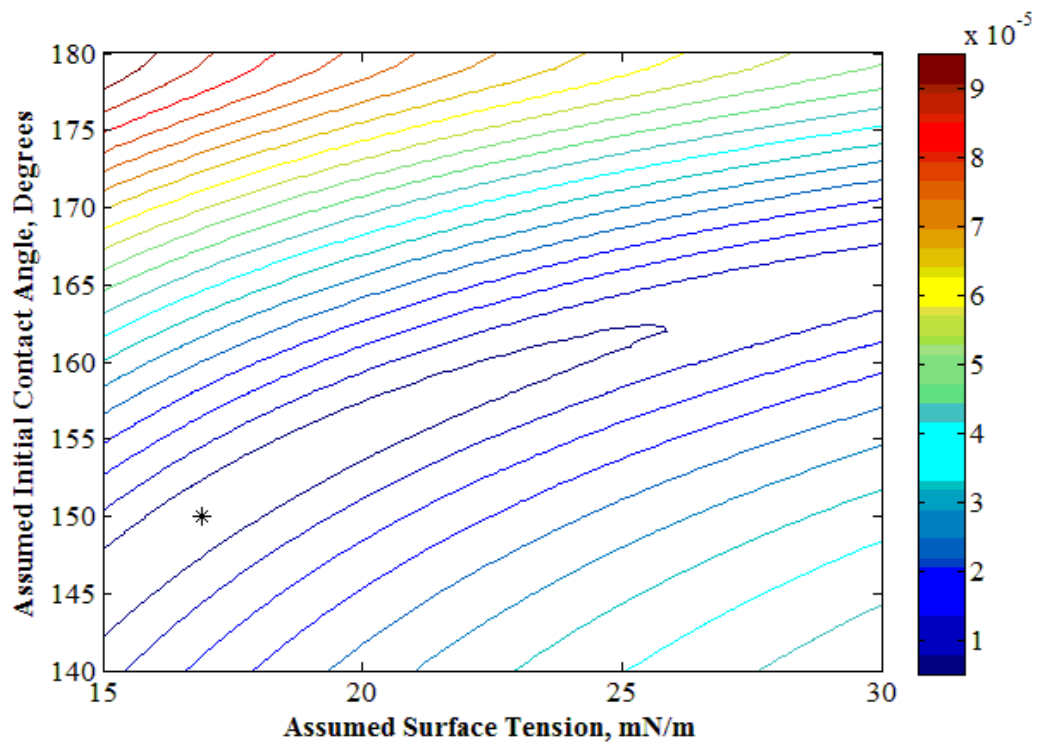


Figure 25: Standard deviation of calculated drop volume as a function of the assumed initial contact angle and surface tension for the hypothetical experiment. The calculated minimum point (16.9, 150) is also shown.

3.4 Conclusion

In this chapter, it is demonstrated the determination of the configuration of a sessile microliter droplet within an electrowetting system through the measurement of the electrical impedance of the wetted area and the analytical modeling of its axisymmetric surface. The experiment consisted of an aqueous capillary bridge extending between two electrodes and surrounded by an ambient oil. Upon the application of a bias voltage, the bridge electrowetted on one electrode surface, leading to an increase in wetted area and a simultaneous bridge morphology change. The wetted area was then directly extracted from the measured impedance. Using the identified wetted area and other known system parameters, we demonstrated that the contact angle as a function of applied voltage can be accurately determined for an electrowetting system without the use of optical measurements. We also found that droplet volume and surface tension could be accurately estimated from impedance data.

By using a batch of impedance data taken at various bias voltages, it is shown that simultaneous identification of several unknown droplet parameters can be carried out. Depending on the parameters to be identified there may be directions in the parameter space with low error sensitivity, making the identification problem fundamentally difficult in this case.

4 Building a High-speed Capacitance Measurement System for Characterizing Dynamic EWOD

4.1 Introduction

As mentioned above, one advantage of electrical measurement is its high speed. Therefore, measuring the capacitance as a function of time provides a useful method to acquire important information about the dynamics of the EWOD process, i.e. the partial wetting physics. Most reported works studying wetting dynamics have used the traditional imaging method [47–50], which typically has a measurement speed of 500 Hz to 1k Hz (500 to 1000 frames per second recording) with expensive video recording equipment. With electrical measurements, it should be possible to increase the measurement and data acquisition speed by at least a factor of 10^2 and at a much lower cost.

Although wetting, including EWOD, has been studied for many years, many fundamental problems remains only partially understood, especially those related to the mechanisms by which a contact line advances or recedes across the solid. Therefore, our ability to predict wetting behaviors and that of processes dependent on wetting is greatly limited. Among the few studies of the dynamic behaviors of the liquid drop, the most popular models for describing the process are:

- The hydrodynamic model, which attributes dissipation to the viscous flow within the wedge of liquid near the contact line. This classic approach fails to describe the liquid flow near the contact line [51] and is empirical. Also noted by Van Mourik et al [52], this model is only valid for advancing contact line (positive contact line velocity) [53].
- The molecular-kinetic (MK) model, which discards the viscous flow idea and

attributes the dissipation to the jumping of molecules along the solid surface [54,55]. This theory is widely considered a better model than the hydrodynamic one.

Among all these studies, efforts have been focused on describing the relationship between the dynamic contact angle and the velocity of the three-phase contact line, and no general description of the base area evolution for partial wetting is achieved. However, the base area change as a function of time is of considerable interest as area can be measured more accurately and the relation is capable of providing direct indications for wetting speed. For example, Lavi and Marmur [57], proposed an exponential power law (EPL) and suggested the kinetics of partial droplet spreading as

$$\frac{A}{A_f} = 1 - \exp\left(-\frac{K}{A_f}\tau^n\right) \quad (22)$$

where A denotes the liquid/solid base area, A_f , K , n are empirical parameters, and τ is the normalized time. This model explained a lot of experimental data successfully over a wide range of capillary numbers, when the popular hydrodynamic and MK model could only work for low capillary numbers.

In their work, fitted empirical parameters n and K showed rough trends with respect to some experimental parameters such as the equilibrium contact angle, the liquid viscosity, and the surface tension. However, more data is needed to establish definitive correlations. By taking time-resolved capacitance measurements during the EWOD process, the base area vs. time relationship could be easily determined and a considerable database could be obtained. Potentially, some extent of physical justification of the empirical model could be made, which would be helpful in predicting the dynamic behavior of various electrowetting systems.

4.2 Circuit Design

With the impedance analyzer HP 4192A and the LabView programming language, the fastest measurement and data acquisition speed that can be achieved is approximately 78 milliseconds per data point, which is far slower than could be achieved with with an optimized acquisition system. The speed is basically limited by two factors: (1) the instrument takes about $\sim 63-67$ ms to conduct the measurement; (2) data acquisition is software timed and serial communication between the PC and the instrument is time-consuming. With this measurement speed, we are missing out on the potential of this technique by failing to capture the impedance changes occurring at fast time scales. Besides, off-the-shelf impedance analyzers employing a GPIB (IEEE-488) interface take measurements at a rate (a few hundred Hz max) far slower than desired for characterizing dynamic properties. Therefore, we have decided to build a custom capacitance measurement and data acquisition system capable of high speed measurements.

The measurement circuit uses a custom-built analog timer to generate a signal whose frequency is inversely proportional to the device capacitance. The circuit schematic is shown in Figure 26. The operation is similar to that of a commercial 555 timer chip operating in astable mode: the EWOD device (capacitor C) charges from V_{cc} through R4 and R5 until its voltage just exceeds V2, then the discharge transistor T1 (n-type MOSFET) goes ON and C discharges through R5 and T1 to ground. When the capacitor voltage drops just below V1, T1 goes OFF and C charges again through R4 and R5. The oscillation on the capacitor is then fed to the RS latch and buffer at the previous stage and becomes a square wave, which can then be received by the micro-controller for frequency measurement and data recording. The corresponding charge and discharge times are: $T_{charge} = (R_4 + R_5) \log(\frac{V_{cc}-V_1}{V_{cc}-V_2})C$ and

$T_{discharge} = R_5 \log(\frac{V_2}{V_1})C$. The total period is

$$T = T_{charge} + T_{discharge} = (R_4 + R_5) \log(\frac{V_{cc} - V_1}{V_{cc} - V_2})C + R_5 \log(\frac{V_2}{V_1})C \quad (23)$$

Therefore, the measured output frequency is

$$f = 1/T = 1/[(R_4 + R_5) \log(\frac{V_{cc} - V_1}{V_{cc} - V_2}) + R_5 \log(\frac{V_2}{V_1})] \cdot \frac{1}{C} \quad (24)$$

and the capacitance of interest can be calculated as

$$C = 1/T = 1/[(R_4 + R_5) \log(\frac{V_{cc} - V_1}{V_{cc} - V_2}) + R_5 \log(\frac{V_2}{V_1})] \cdot \frac{1}{f} \quad (25)$$

where V_{cc} , V_1 , V_2 , R_4 , and R_5 are known design parameters. Therefore, device capacitance and the corresponding wetting area data can be easily calculated with measured frequency data.

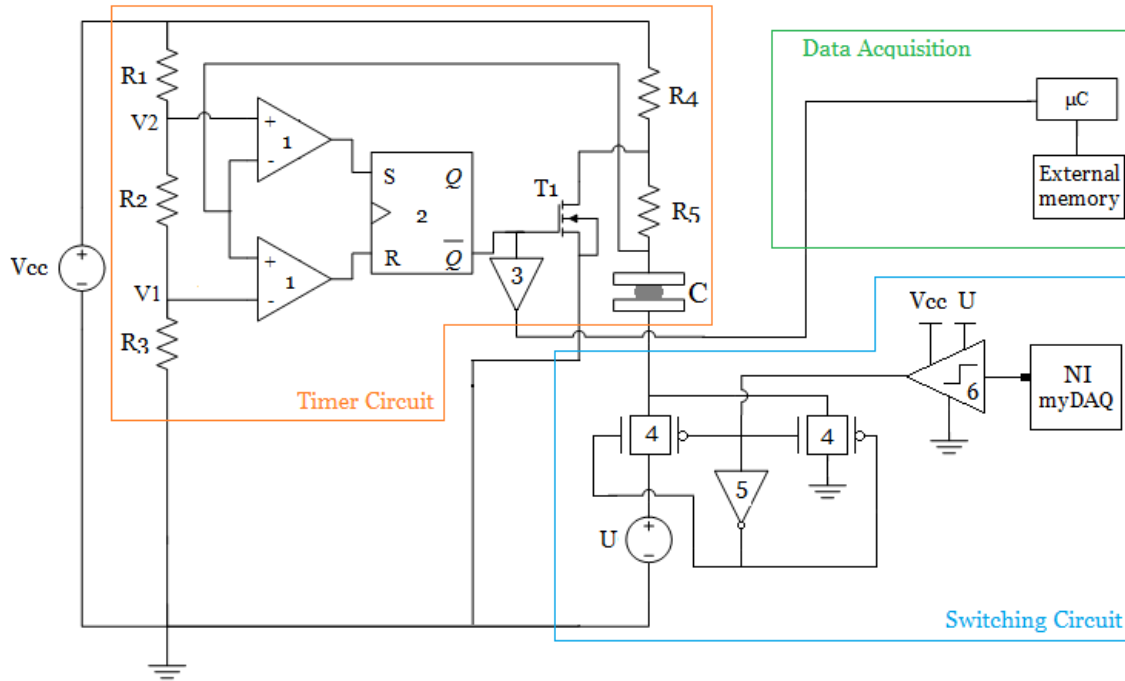


Figure 26: Circuit schematic of the custom-built capacitance measurement system.

Our circuit is different from the commercial 555 timer in that the comparator trigger points, $V1$ and $V2$, are set (through voltage divider $R1, R2$, and $R3$) such that the voltage swing appearing at the device is sufficiently small (~ 100 mV). It is done so the voltage swing added to the device will not influence device performance. The driving voltage for the device (U) is provided by a power supply (HP 3631A Triple Output DC Power Supply) connected in series. The presence or change of $U2$ does not affect the performance of the capacitance measurement circuit.

However, when programmed with LabView, the voltage step $0-U$ provided by the regulated DC power supply has a relatively long transient time. Figure 27 shows the oscilloscope capture of a $0-10$ V voltage step generated by the power supply. It can be seen that a single voltage step took approximately 10 ms to reach its final level, which makes it difficult to rule out the influence of the applied bias change when projecting EWOD dynamic behavior.

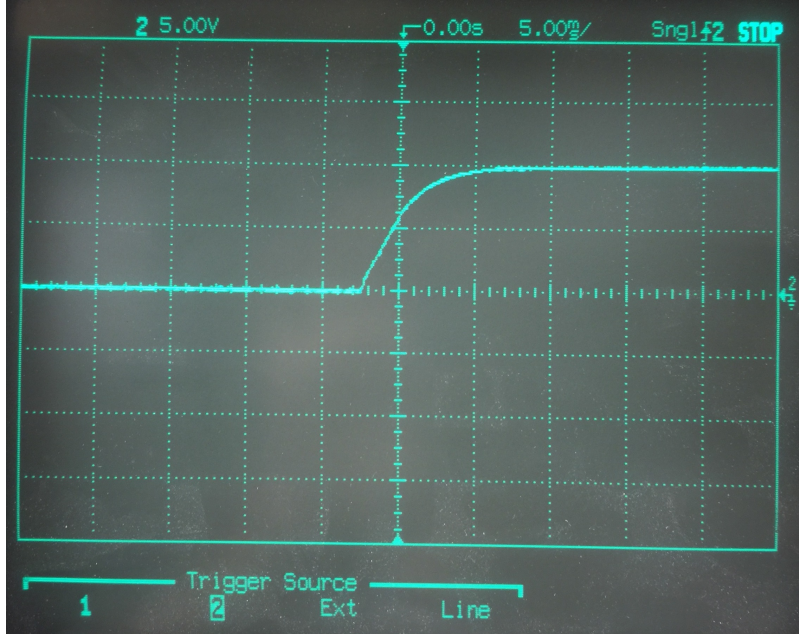


Figure 27: Oscilloscope capture of a 0-10V voltage step generated by the HP3631A DC power supply.

Therefore, we designed a switching circuit (shown in Figure 26) to solve this problem. The circuit has two transmission gates (“4”) controlled by two complementary signals, which is generated by one of the digital output port of the NI myDAQ card. The digital output has an amplitude of 3.3V, and this signal goes through a level converter (“6”) to be converted to U before reaching the gate of the transmission gates. Therefore, when the myDAQ card outputs digital “0” (0V), the transmission gate on the right goes ON and the one on the left goes OFF, making the device charges and discharges to ground; when the myDAQ outputs “1” (3.3V), the transmission gate on the left goes ON and DC bias “U” is applied to the device. Because the myDAQ digital output can switch between “0” and “1” rapidly (transient ~ 50 ns), the bias U can be applied to the EWOD device much faster.

A list of IC components used to build the circuit is shown in Table 4. The numbering of the components corresponds to that marked in Figure 26. These components

were chosen based on several parameters including logic, propagation delay, and power range.

Table 4: A list of IC components used in the capacitance measurement circuit.

Numbering	Logic	Part Number	General Description
1	Comparator	MAX942	high-speed, low-power, 3V/5V, rail-to-rail, single-supply comparator
2	NAND Gate	SN74AC00N	quadruple 2 input positive NAND gates
3	Buffer	SN74HC125N	quadruple bus buffer gates with 3-state outputs
4	Transmission Gate	ADG452B	LC ² MOS 5Ω R _{ON} SPST switches
5	Inverter	CD4069UBE	CMOS hex inverter
6	Level Converter	CD40109BE	CMOS quad low-to-high voltage level shifter
T1	N-Type MOSFET	5LN01SP	N-channel small signal MOSFET

4.3 Frequency Measurement and Data Acquisition

4.3.1 Frequency Measurement

As illustrated in Section 4.2, device capacitance can be transformed into the frequency of a square wave to be measured and calculated. And the way we used to measure the frequency is feeding the pulse train into a micro-controller and measuring the period. In this way, one capacitance data can be acquired in every single period of the signal, and the measurement speed is essentially the same as the measured frequency.

The micro-controller we used is a TMS320F28377S from Texas Instruments (TI). This 32-bit microcontroller unit (MCU) is based on TI's 32-bit C28x floating-point CPU, which provides 200 MHz of signal processing performance. [58] In addition, this MCU features several performance analog and control peripherals including six enhanced capture modules (eCAP), one of which is used for the frequency measurement. Each eCAP module can be configured to operate in Difference (Delta) mode, which is convenient for period and duty cycle measurements of pulse train signals. It also consists of 4 32-bit time-stamp capture registers (CAP1-CAP4), which are capable of continuously storing measured data.

Figure 28 illustrates the capture sequence of the eCAP module for collecting Delta timing data from a pulse train waveform. At each rising edge of the signal, the contents of the counter (CTR) is first captured and stored in CAP_i ($i=1,2,3,4$), then CTR is reset to zero. At the next rising edge (also called capture event, CEVT), the CTR content, which is the number of clock cycles counted between these two edges, is also captured and stored in CAP_{i+1} . The Mod4 counter (MOD4 CTR), which keeps track of the value of "i", will wrap around if the eCAP module is set to work in continuous mode. When all four CAP registers are loaded with measured data, an

interrupt can be generated and the four data points can be read out and stored in an array in on-chip SRAM for further data acquisition.

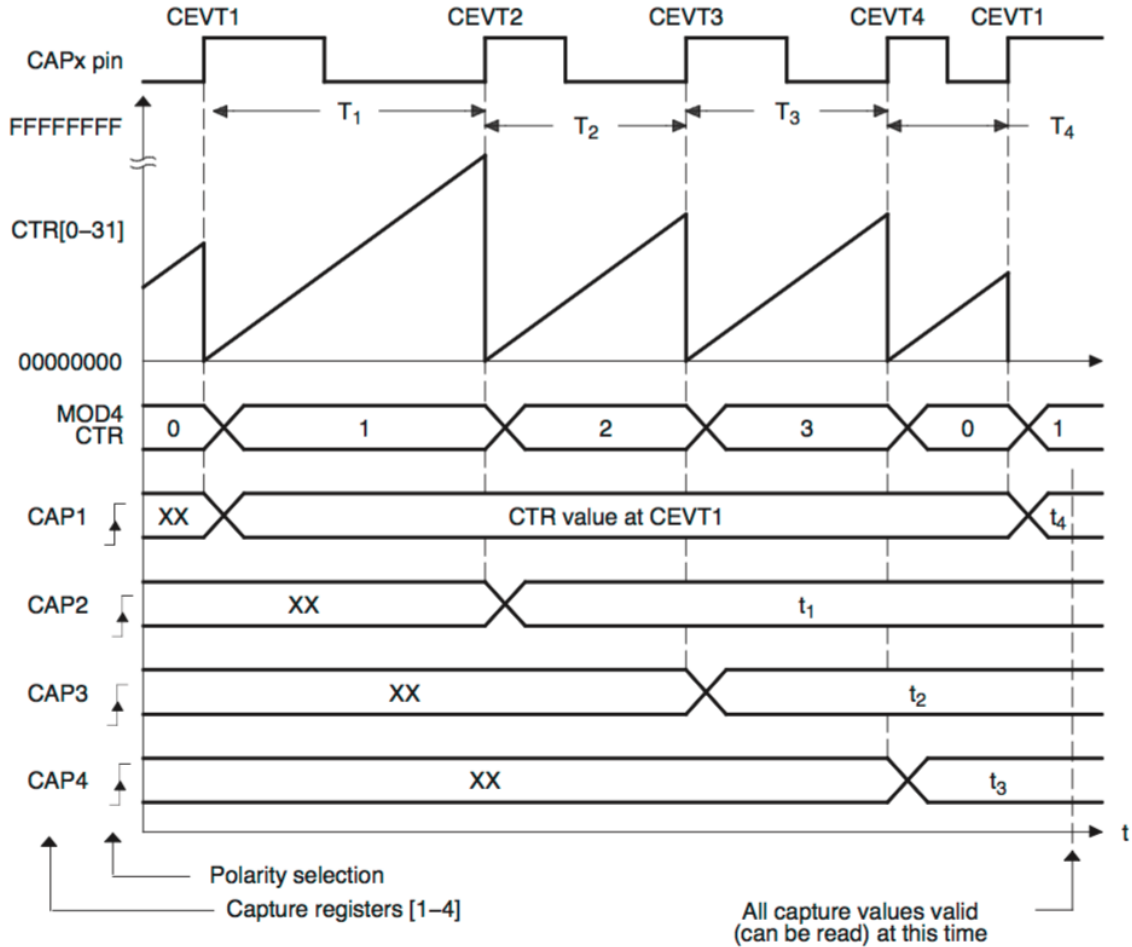


Figure 28: TI TMS320F28377S eCAP module capture sequence for delta mode timestamp and rising edge trigger. [59]

4.3.2 Data Acquisition

As illustration in the previous section, with the way we measure capacitance, we are getting one data point in every period of the signal. Therefore, the faster our measurement speed is, the more data points we get. For example, for a measurement speed of 100kHz, we will get 100K data points every second. Assuming every data point takes one byte (8 bits), 1 second of measurement will generate 100 KB of

data. While almost all micro-controllers have very limited on-chip RAM space for data storage (132 KB for the TMS320F28377S), we need to output the acquired data quickly while performing measurement.

Since the TI TMS320F28377S micro-controller is equipped with several Serial Peripheral Interface (SPI) peripherals, the fastest way to output data would be interfacing the micro-controller with a Secure Digital (SD) type or Multi-Media Card (MMC) type of flash memory card. SD, being introduced in 1999 as an improvement over MMC, is a non-volatile memory card format developed by the SD Card Association [60]. An SD card comes with nine edge connectors and can connect to the host through SPI or four bit parallel (SD) mode. The interface mode is selected at power up and cannot be changed before power down. An SD card operates within a supply range of 2.0 to 3.6 V, which is compatible with our micro-controller. With the release of SD specification version 2.0, SD card data transfer rate is increased to 25MB/sec and clock speed is increased to 50 MHz. [61] The interconnection between the TMS320F28377S and the SD card is illustrated in Figure 24.

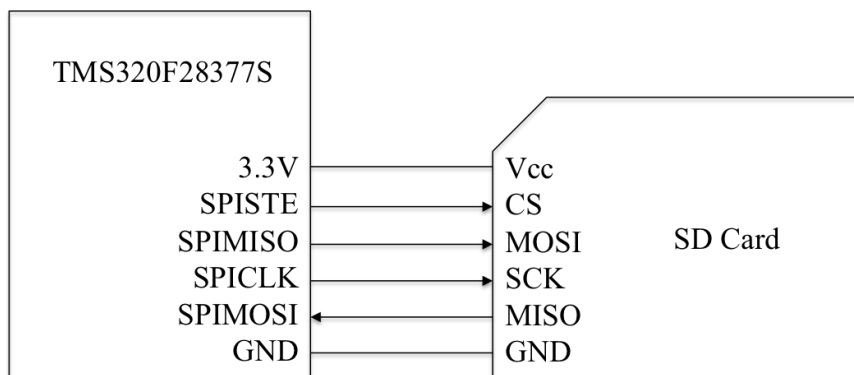


Figure 29: Interconnection schematic between the TMS320F28377S micro-controller and SD card in SPI mode.

Actual connections were made with jumper wires between the micro-controller and a commercial SD breakout board. The breakout board comes with a card socket, pull-

up resistors, and corresponding pin-out for easy connection. A picture of the actual connection is shown in Figure 30. The SD card is powered by the micro-controller's 3.3V source, and the four pins for SPI communication, i.e. CLK (clock), MOSI (master-out slave-in), MISO (master-in slave-out), and CS (chip select or enable) are also connected accordingly.

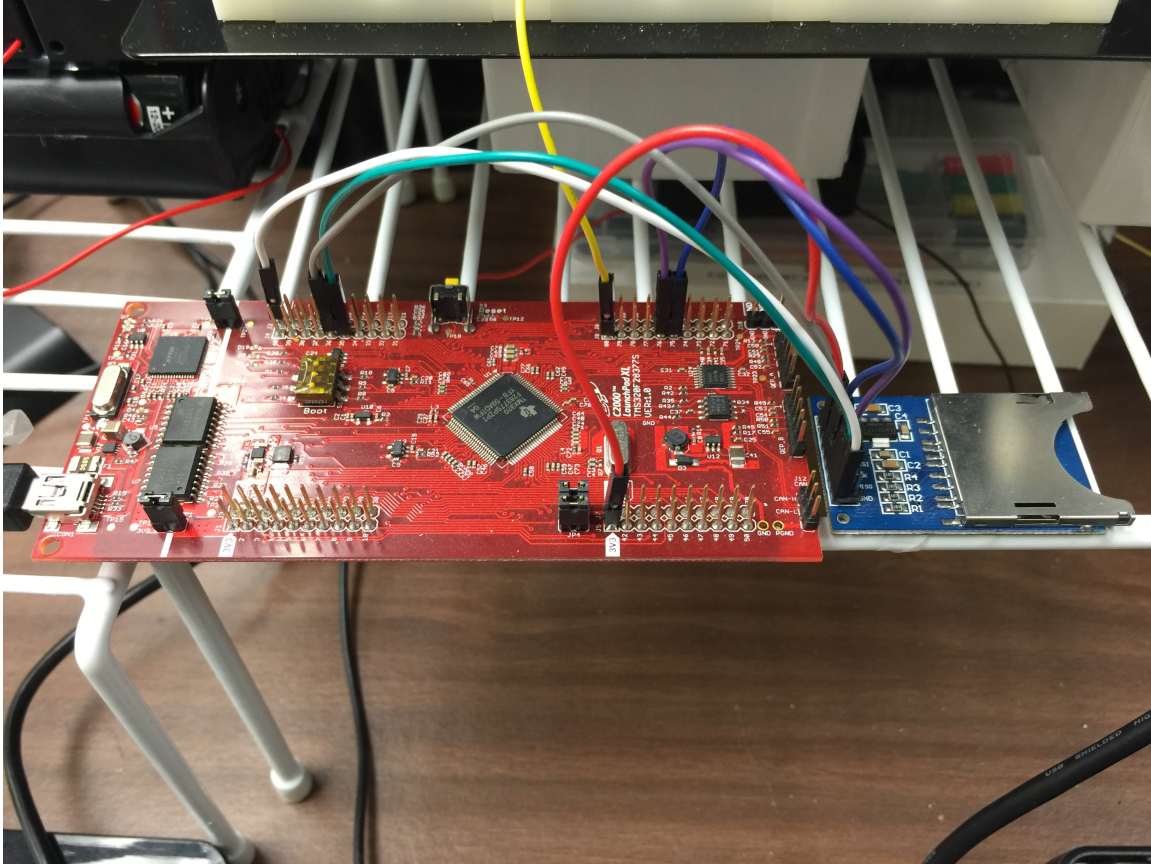


Figure 30: Actual interconnection between the TMS320F28377S micro-controller and SD card.

Software is developed with C, using TI's Code Composer Studio 6.1.2. Figure 31 shows the code design flow.

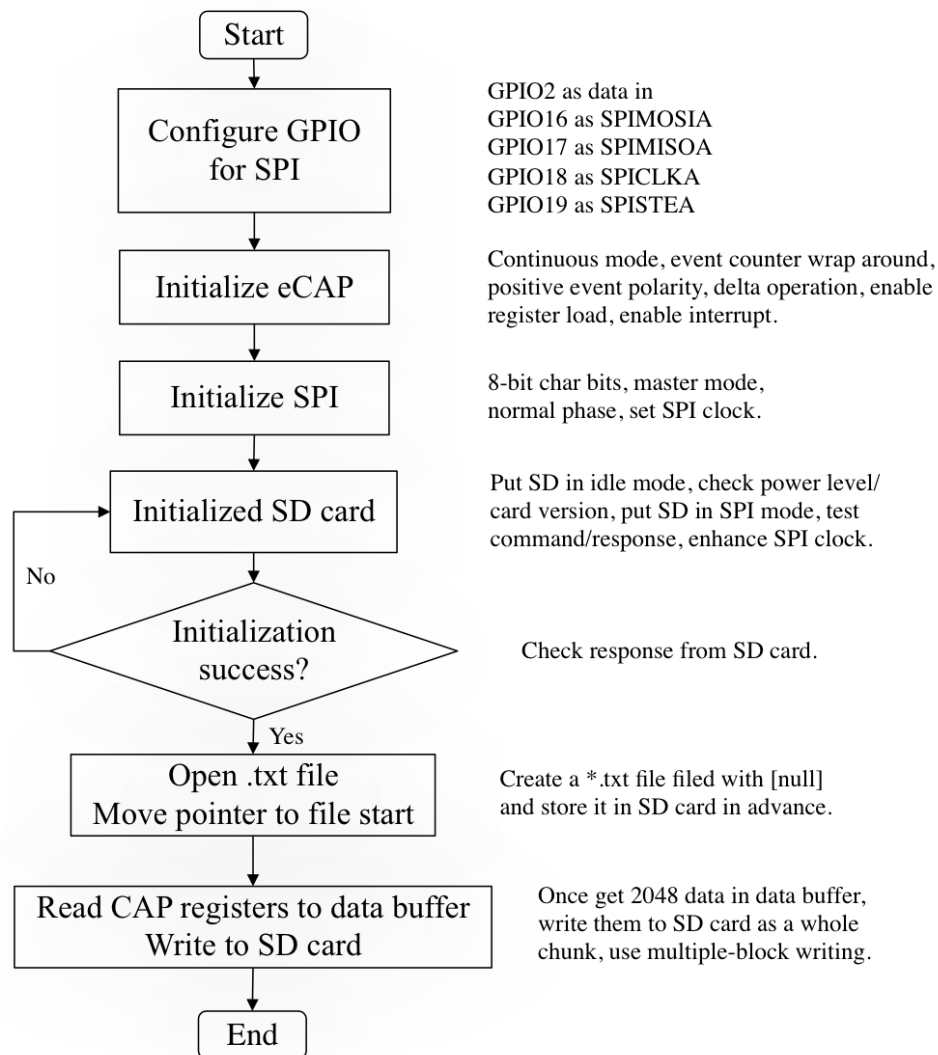


Figure 31: Software design flow for frequency measurement and data acquisition.

After the micro-controller is powered up, GPIO configuration for SPI is first performed. In addition, GPIO2 is configured as input to take the signal to be measured by the eCAP module. Following the GPIO configuration, the eCAP module and the SPI module are initialized by setting desired operation mode. Here the SPI transmission length is set to be 8 bits as the data format will be set to "char" (8 bits) in order to store more data. The device peripheral initialization functions can be

found in the "main.c" file (Appendix A). SD card initialization is then performed. There is a fixed sequence for card initialization and the procedure can be found in the SD specifications [61]. During card initialization, SPI baud rate is first set to a low value (less than 400 Hz). Then CS is held high and the SPI transmits 0xFF00 ten times to force DI (Data In) of the card to be held high for 80 clock cycles as required by card power-up initialization. Next, a sequence of commands are sent to ask the card to go into idle state and determine its version. If the card initialization is succeeded, SPI baud rate is then set to a high value for actual data transmission. The SD initialization function can be found in "mmc.c" (Appendix B). The measured data points are first read out from the eCAP registers (CAP1-CAP4) and stored in a data buffer. When the data buffer is full, these data are then transmitted to the SD card as an entire chunk. The "write to SD card" operation is performed with the Generic FAT File System (FatFs) module introduced by Elm Chan [62]. The FatFs is in compliance with ANSI C and is platform independent. Data are written to a pre-defined text file in the SD card as ASCII characters, and are translated to numbers later using Python (Appendix C).

4.4 Results and Analysis

We then measured an EWOD device with the custom capacitance measurement system. The device has a parallel configuration similar to that in Figure 27. A conductive aqueous droplet (0.1M Cs_2SO_4) is sandwiched between a thin dielectric (Al_2O_3) covered aluminum plate and a gold-coated silicon wafer. In this structure, the contact line is pinned on the conducting gold plate and electrowetting occurs on the dielectric side.

The measured capacitance-time response to a 0-7 V and 7-0 V step input is shown in Figure 32. Each data point represents the average of ten individual measurements. The raw data rate in this experiment is approximately 110kHz (~ 11 kHz for the averaged results); this is considerably faster than typically obtained with general-purpose impedance analyzers (for example, ~ 13 Hz for an HP 4192A limited by the GPIB). Higher measurement rates are possible by changing the RC time constant established by the device and resistors R4 and R5. The resistor values used in this test is $R4=3.54\text{k}\Omega$ and $R5=8.04\text{k}\Omega$. In response to the 0-7V voltage step, the drop spreads out quickly, approaching steady state in approximately 0.2s, which is similar to that reported in [47, 50, 63].

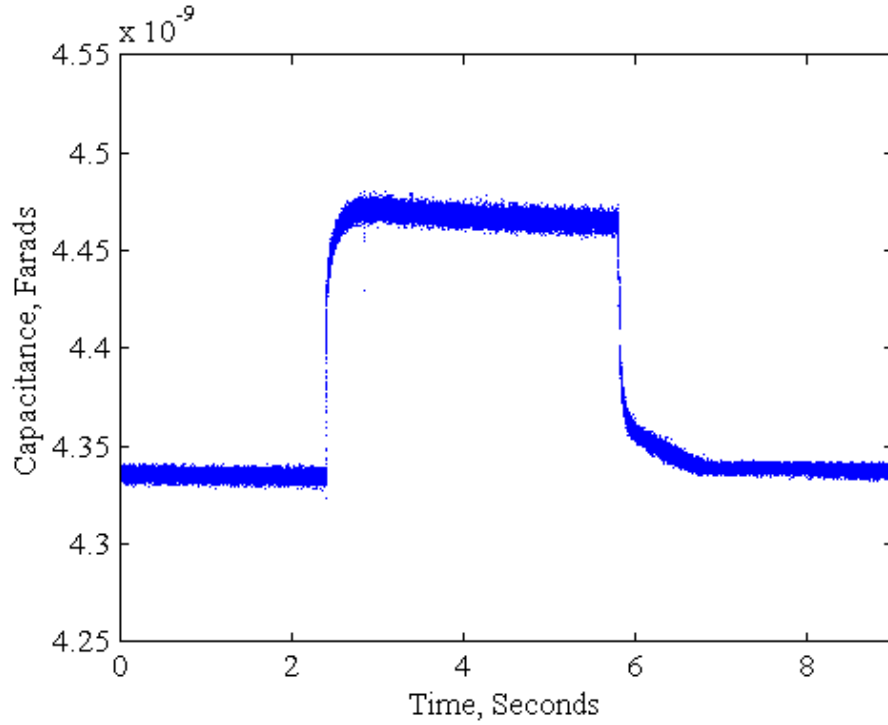


Figure 32: Capacitance-time data in response to a 0-7V and 7-0 V step input. Each data point is the average of ten capacitance measurements.

The drop radius change during the transient determined from the capacitance data and was fitted with a sum of exponentials using nonlinear optimization (Figure 33). Time constants associated with the best fit were found to be $\tau_1=0.005s$ and $\tau_2=0.098s$. The oscillatory behavior in the measured data is mainly due to the 60 Hz hum. An analytical derivative of the function yields the estimated contact line speed and is plotted in Figure 34. The speed sees no oscillation as reported in [26] and decreases quickly after reaching its highest value, which is on the order of 2mm/s.

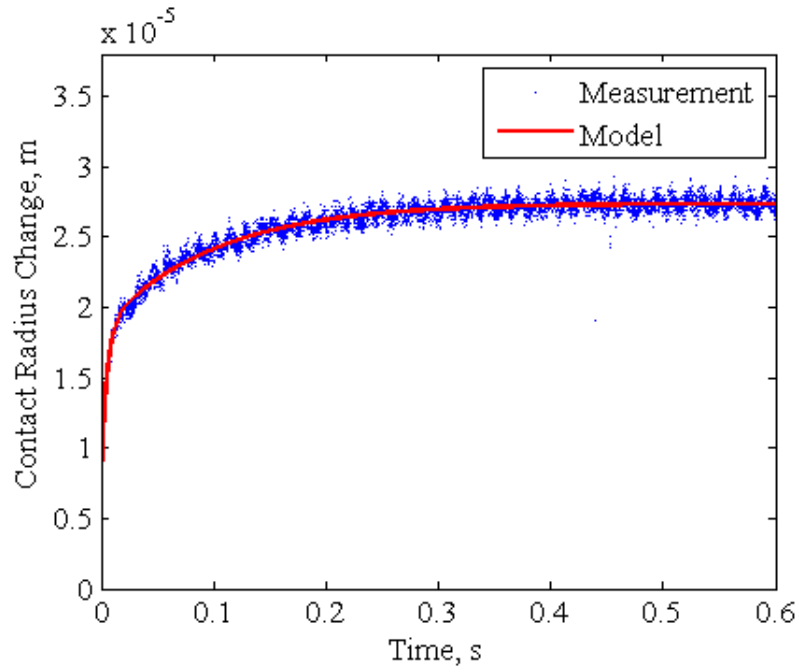


Figure 33: Drop radius change during the transient determined from the measured capacitance data.

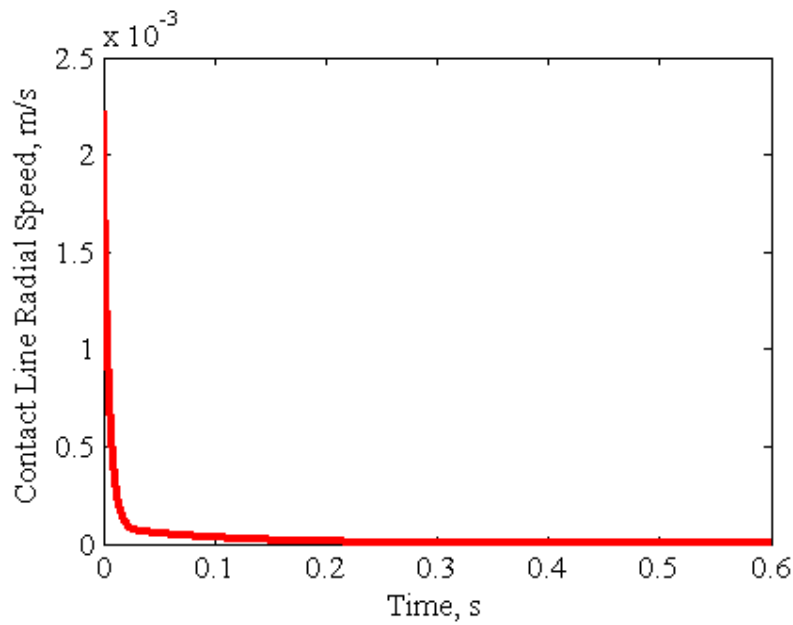


Figure 34: Radial speed of the contact line calculated from the fitted model for radius change.

4.5 Evaluation of the Measurement System

This way of measuring frequency is essentially a digital method. The recorded data, i.e. the count, are calculated as the ratio of the CPU clock frequency and the circuit's output frequency and can only be integers. Therefore, the resolution of the measurement depends on these two frequencies. When configuring the eCAP module, the counter clock is sourced from the system clock, which is set to the maximum value of 200 MHz. Note that 200 MHz is also the highest clock frequency available in commercial micro-controllers.

Recalling Equation (25):

$$C = 1/T = 1/[(R_4 + R_5) \log\left(\frac{V_{cc} - V_1}{V_{cc} - V_2}\right) + R_5 \log\left(\frac{V_2}{V_1}\right)] \cdot \frac{1}{f} \quad (25)$$

we know that capacitance C is a function of V_{cc} , V_1 , V_2 ($V_2=V_1+100\text{mV}$), R_4 , and R_5 . For a certain V_{cc} , a certain sample (fixed C), and fixed R_4 and R_5 , the measurement speed (output frequency) and capacitance resolution can be calculated and an example is plotted in Figure 35. As can be seen, measurement speed is positively correlated with V_1 . When $V_1 > 0.46\text{V}$, measurement speed can reach a value that is higher than 100 kHz, while corresponding capacitance resolution is roughly between 3 pF and 7 pF. In real experiments, V_1 can be chosen based on measurement speed and resolution requirement. In general, the lower V_1 is, the better the resolution we get yet the slower the measurement is carried out.

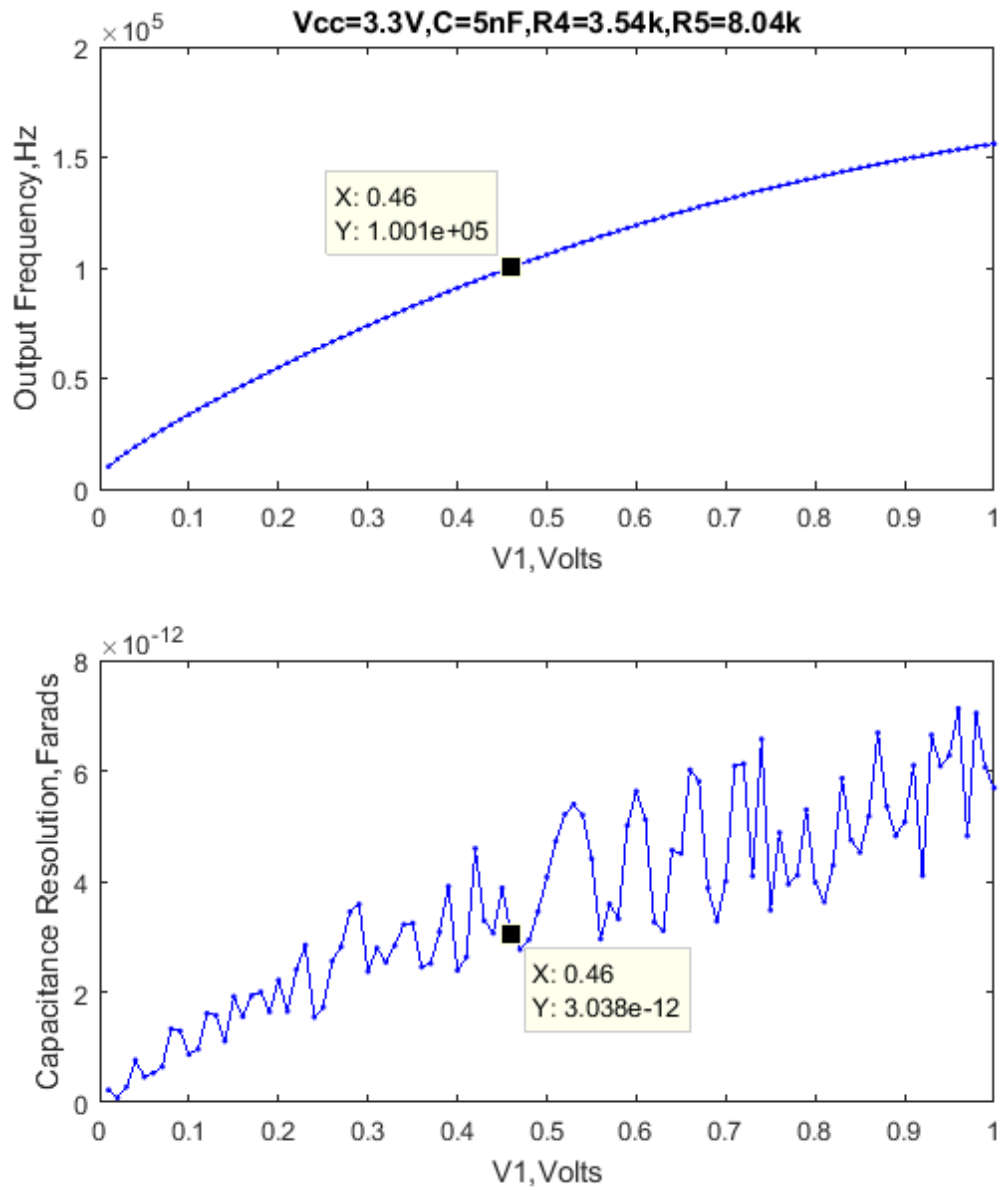


Figure 35: Measurement speed and capacitance resolution as a function of V_1 .

Besides the digitizing of measurement, signal jitter can also result in error. This is because the voltage swing on the capacitor has been minimized to ~ 100 mV, and only a few mV of noise on the power supply can have an outsized effect and change the timing a lot. This cause had been experimentally confirmed by powering the circuit with batteries. Therefore, we used very short leads (about 1 to 2 inches long) in the

power and ground path from the power supply to the circuit board to minimize signal jitter. In most of our experiments, the jitter observed is less than 0.5 kHz, which is an error less than 0.5% for a measuring speed of 100 kHz.

Some other error sources include the parasitic capacitance on the comparator input pins (typically a few picofarads), finite discharge FET on-resistance, comparator timing variation, etc. For the measured capacitance of a few nanofarads (our typical thin-film EWOD samples), these errors are generally very small and can be ignored.

5 Conclusion and Future Work

In this work, the method of using impedance spectroscopy in characterizing low-voltage EWOD is explored.

5.1 Impedance Spectroscopy of EWOD Devices

First of all, the electrical properties of interface elements in typical thin-film EWOD configurations were examined and analyzed using impedance spectroscopy:

- The wire electrode/liquid interface and planar electrode/liquid interface exhibited electric double layer(EDL) behavior which was well modeled with a constant phase element (CPE) model.
- The planar dielectric/liquid interface comprises a series combination of the dielectric capacitance and EDL, but exhibited first order RC behavior due to the dominance of the dielectric capacitance over the EDL.

With the individual elements examined and well modeled, the impedance of three most commonly seen EWOD setups with thin dielectrics were investigated as a function of frequency:

- For a conventional setup with an inserted wire electrode, the EDL at the wire dominates the total impedance spectra of the system, making it difficult to characterize EWOD with electrical measurements.
- For a parallel plate setup with one plate bare and the other covered with dielectric, the dielectric capacitance dominates the total impedance spectra when the wetting areas at both plates are comparable.

- For a parallel plate setup with both electrodes covered with dielectric, the system impedance is dominated by the series combination of these dielectric capacitance and the EDL elements can be ignored.

Therefore, in order to characterize thin-film EWOD devices electrically, setups need to be properly designed so that the dielectric capacitance dominates the total impedance spectra of the device. In general, this can be achieved for parallel plate configurations even with nanometer thick thin-films; while for inserted wire setups the surface area of the wire need to be greatly enhanced.

5.2 Interrogation of Droplet Configuration

Based on the study of the electrical behaviors of thin-film EWOD devices with fixed wetting area, methods were developed to use electrical measurements in conjunction with known capillary bridge geometries to determine unknown parameters during electrowetting. With an example EWOD setup where an aqueous capillary bridge extends between two planar electrodes, the changes in wetted area upon the application of a DC bias were directly extracted from measured capacitance data. Using the identified wetted area and other known system parameters, it is demonstrated that the contact angle as a function of applied voltage can be accurately determined for an electrowetting system without the use of optical measurements. In addition, other parameters such as the droplet volume and surface tension could be accurately estimated from the impedance data.

As current code for modeling bridge shape and computing relevant parameters utilizes default root-finding functions in Mathematica and can be time-consuming and difficult under some circumstances, possible future work includes the optimization of algorithm and code in order to achieve faster computation and better tolerance for input parameters.

5.3 High-speed Capacitance Measurement System

In the end, a capacitance measurement system capable of high-speed time-resolved measurements of electrowetting behavior was designed, built, and tested. The test circuit contained a custom-built analog timer which generated a frequency that is inversely proportional to the measured capacitance. Voltage swing applied to the device was minimized in order not to affect device performance. The generated pulse train was then fed into a 32-bit micro-controller unit for frequency measurement and data acquisition. Corresponding software was also developed and tested. Dynamic electrowetting was measured with this system at the speed of 100 kHz to 150 kHz. The transient response of the device to a single voltage step was also analyzed and modeled.

The measured data was analyzed in the frequency domain and the result suggested 60 Hz hum and pink noise. Preliminary tests showed that the 60 Hz hum was induced by contaminated earth ground, therefore powering the test circuit off batteries and using opto-isolator between the circuit and the micro-controller should eliminate the problem. As for the pink noise, using precision components such as metal foil resistors and better ICs could possibly reduce the noise and improve resolution.

With this measurement system, a considerable amount of data regarding the dynamic behaviors of various EWOD systems could be quickly obtained without the hassle of using expensive video recording equipment. By taking tests of various EWOD devices with different physical parameters such as surface tension, liquid viscosity, and drop size, some extent of physical justification of the empirical model could potentially be made.

References

- [1] F. Mugele and J. Baret. (2005). Electrowetting: from basics to applications. *Journal of Physics: Condensed Matter*. 17(28), pp. R705.
- [2] Shamaï, Romi, et al. (2008). Water, electricity, and between... On electrowetting and its applications. *Soft Matter*. 4(1), pp. 38-45.
- [3] M. G. Lippman. (1875). RCouche double. Electrocapillarit. Surtension. *Actualités Scientifiques*. 373, pp. 5-36.
- [4] A. Froumkine. (1936). Relations entre les ph'énomènes électriques et capillaires. *Annales de Chimie et de Physique*. 5, pp. 494-548.
- [5] B. Berge. (1993). Electrocapillarit et mouillage de films isolants par l'eau. *C.R.A.S. III*. 317, pp. 157-163.
- [6] B. Berge and J. Peseux. (2000). Variable focal lens controlled by an external voltage: An application of electrowetting. *The European Physical Journal E*. 3(2), pp. 159-163.
- [7] S. Kuiper and B. H. W. Hendriks. (2004). Variable-focus liquid lens for miniature cameras. *Applied Physics Letters*. 85(7), pp. 1128-1130.
- [8] T. Krupenkin, S. Yang, and P. Mach. (2003). Tunable liquid microlens. *Applied Physics Letters*. 82(3), pp. 316-318.
- [9] C. B. Gorman, H. A. Biebuyck, and G. M. Whitesides. (1995). Control of the shape of liquid lenses on a modified gold surface using an applied electrical potential across a self-assembled monolayer. *Langmuir*. 11(6), pp. 2242-2246.

- [10] B. Berge. Liquid lens technology: principle of electrowetting based lenses and applications to imaging. *Micro Electro Mechanical Systems, 2005. MEMS 2005. 18th IEEE International Conference on.* pp. 227-230. IEEE, 2005.
- [11] R. B. Fair. (2007). Digital microfluidics: is a true lab-on-a-chip possible?. *Microfluidics and Nanofluidics.* 3(3), pp. 245-281.
- [12] Z. Wan, H. Zeng, and A. Feinerman. (2006). Area-tunable micromirror based on electrowetting actuation of liquid-metal droplets. *Applied Physics Letters.* 89(20), pp. 201107.
- [13] P. Mach, et al. (2002). Dynamic tuning of optical waveguides with electrowetting pumps and recirculating fluid channels. *Applied Physics Letters.* 81(2), pp. 202-204.
- [14] F. Mugele, J. C. Baret, and D. Steinhauser. (2006). Microfluidic mixing through electrowetting-induced droplet oscillations. *Applied Physics Letters.* 88(20), pp. 204106-204106.
- [15] N. Vergauwe, et al. (2011). A versatile electrowetting-based digital microfluidic platform for quantitative homogeneous and heterogeneous bio-assays. *Journal of Micromechanics and Microengineering.* 21(5), pp. 054026.
- [16] R. B. Fair, et al. A micro-watt metal-insulator-solution-transport (MIST) device for scalable digital bio-microfluidic systems. *International Electron Devices Meeting.* pp. 367-370. IEEE; 1998,2001.
- [17] S. K. Cho, et al. (2003). Creating, transporting, cutting, and merging liquid droplets by electrowetting-based actuation for digital microfluidic circuits. *Microelectromechanical Systems, Journal of.* 12(1), pp. 70-80.

- [18] P. Y. Paik, V. K. Pamula, and K. Chakrabarty. (2008). A digital-microfluidic approach to chip cooling. *Design & Test of Computers, IEEE. 25(4)*, pp. 372-381.
- [19] K. Pettigrew, et al. Performance of a MEMS based micro capillary pumped loop for chip-level temperature control. *Micro Electro Mechanical Systems, 2001. MEMS 2001. The 14th IEEE International Conference on.* pp. 427-430. IEEE, 2001.
- [20] K. Mohseni. Effective cooling of integrated circuits using liquid alloy electrowetting. *Semiconductor Thermal Measurement and Management Symposium, 2005 IEEE Twenty First Annual IEEE.* pp. 20-25. IEEE.
- [21] V. K. Pamula and K. Chakrabarty. Cooling of integrated circuits using droplet-based microfluidics. *Proceedings of the 13th ACM Great Lakes symposium on VLSI.* pp. 84-87. ACM, 2003.
- [22] P. Paik, V. K. Pamula, and K. Chakrabarty. Thermal effects on droplet transport in digital microfluidics with applications to chip cooling. *Thermal and Thermomechanical Phenomena in Electronic Systems, 2004. IThERM'04. The Ninth Intersociety Conference on.* pp. 649-654. IEEE, 2004.
- [23] R. A. Hayes and B. J. Feenstra. (2003). Video-speed electronic paper based on electrowetting. *Nature. 425(6956)*, pp. 383-385.
- [24] J. Heikenfeld and A. J. Steckl. (2005). High-transmission electrowetting light valves. *Applied Physics Letters. 86(15)*, pp. 151121.
- [25] H. Moon, S. K. Cho, and R. L. Garrell. (2002). Low voltage electrowetting-on-dielectric. *Journal of Applied Physics. 92(7)*, pp. 4080-4087.

- [26] H. J. J. Verheijen and M. W. J. Prins. (1999). Contact angles and wetting velocity measured electrically. *Review of scientific instruments*. 70(9), pp. 3668-3373.
- [27] H. Ren, R. B. Fair, and M. G. Pollack. (2004). Automated on-chip droplet dispensing with volume control by electro-wetting actuation and capacitance metering. *Sensors and Actuators B: Chemical*. 98(2), pp. 319-327.
- [28] F. Su, S. Ozev, and K .Chakrabarty. (2005). Ensuring the operational health of droplet-based microelectrofluidic biosensor systems. *Sensors Journal, IEEE*. 5(4), pp. 763-773.
- [29] F. Su, S. Ozev, and K .Chakrabarty. (2006). Concurrent testing of digital microfluidics-based biochips. *ACM Transactions on Design Automation of Electronic Systems*, 11(2), pp. 442-464.
- [30] J. Gong. (2008). All-electronic droplet generation on-chip with real-time feedback control for EWOD digital microfluidics. *Lab on a Chip*. 8(6), pp. 898-906.
- [31] H. Ren and R. B. Fair. (2002). Micro/nano liter droplet formation and dispensing by capacitance metering and electrowetting actuation. *Nanotechnology, 2002. IEEE-NANO 2002. Proceedings of the 2002 2nd IEEE Conference on*, pp. 369-372.
- [32] Z. Stojek. 2010. *Electroanalytical methods*. (Berlin Heidelberg: Springer). pp. 3-9.
- [33] T. Pajkossy. (2005). Impedance spectroscopy at interfaces of metals and aqueous solutions- Surface roughness, CPE and related issues. *Solid State Ionics*. 176(25), pp. 1997-2003.
- [34] S. H. Liu. (1985). Fractal model for the ac response of a rough interface. *Physical Review Letters*. 55(5), pp. 529.

- [35] T. Pajkossy. (1997). Capacitance dispersion on solid electrodes: anion adsorption studies on gold single crystal electrodes. *Solid State Ionics*. *94(1)*, pp. 123-129.
- [36] C. H. Hamann and A. Hamnett. 1998. *Electrochemistry*. (Weinheim: Wiley-VCH) pp. 123-124.
- [37] K. Zhou, et al. (2009) A full description of a simple and scalable fabrication process for electrowetting displays. *Journal of Micromechanics and Microengineering*. *19(6)*, pp. 065029.
- [38] F. E. Terman. 1943. *Radio Engineers' Handbook*. (New York: McGraw-Hill). p. 37.
- [39] L. Zubietta and R. Bonert. (2000). Characterization of double-layer capacitors for power electronics applications. *Industry Applications, IEEE Transactions on*. *36(1)*, pp. 199-205.
- [40] P. Kralchevsky, and K. Nagayama. (2001). Capillary bridges and capillary bridge forces. in *Particles at Fluid Interfaces and Membranes*, 1st ed. Amsterdam, The Netherlands: Elsevier, 2001, pp. 469-498.
- [41] J. Plateau. *Statique Experimentale et Theoretique des Liquides Soumis aux Seules Forces Moleculaires*, Gauthier-Villars, Paris, 1873.
- [42] S. Chevalliot, J. Heikenfeld, L. Clapp, A. Milarcik, and S. Vilner. (2011). Analysis of nonaqueous electrowetting fluids for displays. *Journal of Display Technology*. *7(12)*, pp. 649-656.
- [43] H. W. Lu. *Fluid Dynamics of an Electrowetting Drop: Theories, Simulations, and Experiments*, Ph.D. dissertation, Dept. Mech. Eng., Univ. of California, Los Angeles, CA, 2007.

- [44] S. A. Nezamoddini, Capillary force actuators, Ph.D. dissertation, Dept. Mech. and Aerosp. Eng., Univ. of Virginia, Charlottesville, VA, 2008.
- [45] [https://en.wikipedia.org/wiki/Tensiometer_\(surface_tension\)](https://en.wikipedia.org/wiki/Tensiometer_(surface_tension))
- [46] T. D. Blake and J. M. Haynes. (1973). Contact-angle hysteresis. *Progress in surface and membrane science*. 6, pp. 125-138.
- [47] C. Decamps and J. D. Coninck. (2000). Dynamics of spontaneous spreading under electrowetting conditions. *Langmuir*, 16(26), pp. 10150-10153.
- [48] W. C. Nelson, P. Sen, and C. J. Kim. (2011). Dynamic contact angles and hysteresis under electrowetting-on-dielectric. *Langmuir*, 27(16), pp. 10319-10326.
- [49] K. L. Wang and T. B. Jones. (2005). Saturation effects in dynamic electrowetting. *Applied Physics Letters*, 86(5), pp. 054104.
- [50] M. Paneru, et al. (2010). Static and dynamic electrowetting of an ionic liquid in a solid/liquid/liquid system. *Journal of the American Chemical Society*. 132(24), pp. 8301-8308.
- [51] H. Li, P. Mani, S. Rossen, and J. Ralston. (2013). Dynamic electrowetting and dewetting of ionic liquids at a hydrophobic solidliquid interface. *Langmuir*. 29(8), pp. 2631-2639.
- [52] S. V. Mourik, A.E.P. Veldman, M. E. Dreyer. (2005). Simulation of capillary flow with a dynamic contact angle. *Microgravity-Science and Technology*. 17(3), pp. 87-93.
- [53] K. M. Zahra, L. Kadem, and A. Dolatabad. (2010). Effects of dynamic contact angle on numerical modeling of electrowetting in parallel plate microchannels. *Microfluidics and Nanofluidics*. 8(1), pp. 47-56.

- [54] T. D. Blake. and J. M. Haynes. (1969). Kinetics of liquidliquid displacement. *Journal of colloid and interface science.* 30(3), pp. 421-423.
- [55] T. D. Blake. (2006). The physics of moving wetting lines. *Journal of Colloid and Interface Science.* 299(1), pp. 1-13.
- [56] W. M. Haynes. 2014-2015. CRC Handbook of Chemistry and Physics, 95th Edition (Boca Raton, FL: CRC Press). pp. 5-73.
- [57] L. Becky and A. Marmur. (2004). The exponential power law: partial wetting kinetics and dynamic contact angles. *Colloids and Surfaces A: Physicochemical and Engineering Aspects,* 250(1), pp. 409-414.
- [58] <http://www.ti.com/product/TMS320F28377S>
- [59] TI TMS320F28377S technical reference
- [60] http://en.wikipedia.org/wiki/Secure_Digital
- [61] Physical Layer Simplified Specifications, SD Specifications, SD Card Association Technical Committee. (Version 1.10 October 2004 and Version 2.00 September, 2006)
- [62] http://elm-chan.org/fsw/ff/00index_e.html
- [63] C. W. Tsao et al. (2008). Dynamic electrowetting on nanofilament silicon for matrix-free laser desorption/ionization mass spectrometry. *Analytical Chemistry.* 80(8), pp. 2973-2981.

List of Publications

- **X. Hu**, C. Barth, M. Mibus, G. Zangari, C. R. Knospe, and M. L. Reed, High-speed and Low-cost Electrical Characterization of Dynamic Electrowetting-on-dielectric, In the 10th International Meeting on Electrowetting (June 19-22, 2016).
- **X. Hu**, M. Mibus, G. Zangari, C. R. Knospe, and M. L. Reed. (2015). Interrogation of Droplet Configuration during Electrowetting via Impedance Spectroscopy. *J. Microelectromech. Syst*, *24(6)*, pp. 2092-2100.
- M. Mibus, **X. Hu**, C. R. Knospe, M. L. Reed, and G. Zangari. (2015). Anodic Metal Oxides for Electrowetting Systems. *Current Nanoscience*, *11(3)*, pp. 333-342.
- **X. Hu**, M. Mibus, C. R. Knospe, G. Zangari, and M. L. Reed. (2015). Impedance spectroscopy and electrical modeling of electrowetting on dielectric devices. *J. Micromech. Microeng.* *25(4)*, pp.045020.
- M. Mibus, *X. Hu*, C. Knospe, M. L. Reed, and G. Zangari. (2014) (Invited) Octadecylphosphonic Acid Self-Assembled Monolayers in Low Voltage Electrowetting-on-Dielectric Systems. *ECS Transactions*. *61(2)*, pp.325-331.
- M. Mibus, C. Jensen, **X. Hu**, C. Knospe, M. L. Reed, and G. Zangari. (2014) Improving dielectric performance in anodic aluminum oxide via detection and passivation of defect states. *Appl. Phys. Lett.* *104(24)*, pp. 244103.
- M. Mibus, **X. Hu**, C. Knospe, G. Zangari, and M. Reed, Dynamic Contact Angles in Low Voltage Electrowetting-On-Dielectric Systems, In 224th ECS Meeting (Oct 27- Nov 1, 2013). Ecs, 2013.
- M. Mibus, C. Jensen, **X. Hu**, C. Knospe, M. L. Reed, and G. Zangari. (2013). Dielectric breakdown and failure of anodic aluminum oxide films for electrowetting systems. *J. Appl. Phys.*, *114(1)*, pp. 014901.
- **X. Hu**, C. Knospe, M. Mibus, G. Zangari, and M. Reed, Two Terminal Impedance Spectroscopy of Electrowetting on Dielectric Test Structures, In 223rd ECS Meeting (May 12-17, 2013). Ecs, 2013.

Appendix A main.c

```
1 #include "F28x_Project.h" // Device Headerfile and Examples Include
   File
2 #include "third_party/fatfs/src/ff.h"
3 #include "third_party/fatfs/src/diskio.h"
4 #include "third_party/fatfs/src/integer.h"
5
6 // Prototype statements for functions found within this file.
7 __interrupt void ecap1_isr(void);
8 void InitECapture(void);
9 void spi_init(void);
10
11 Uint32 ECap1IntCount=0;
12 Uint32 WriteCount=0;
13
14 WORD index=0;
15 unsigned char diff_array[2560];
16
17 FRESULT res;
18 static FATFS fs; //File system object
19 static FIL fil;
20 WORD bw=0;
21 Uint32 AccStringLength=0;
22
23 void main(void)
24 {
25
26 // Step 1. Initialize System Control:
27   InitSysCtrl();
28
29 // Step 2. Initialize GPIO:
30   InitECap1Gpio(2);
31   GPIO_SetupPinOptions(2, GPIO_INPUT, GPIO_ASYNC); //GPIO2=Pin80
32   InitSpiaGpio();
33
34 // Step 3. Clear all __interrupts and initialize PIE vector table:
35   DINT;
36
37 // Initialize the PIE control registers to their default state.
38   InitPieCtrl();
39
40 // Disable CPU __interrupts and clear all CPU __interrupt flags:
41   IER = 0x0000;
42   IFR = 0x0000;
43
44 // Initialize the PIE vector table.
45   InitPieVectTable();
46
47   EALLOW;
48   PieVectTable.ECAP1INT = &ecap1_isr;
```



```

49     EDIS;
50
51 // Step 4. Initialize the Device Peripherals:
52 InitECapture();
53 spi_init();      // init SPI
54 //DELAY_US(50);
55     if ( res == FR_OK ){
56         res = f_mount(0, &fs);
57         //DELAY_US(100);
58         if ( res == FR_OK ) {
59             res = f_open(&fil, "LOG.txt", FA_WRITE);
60             //DELAY_US(100);
61             if ( res == FR_OK ) {
62                 res = f_lseek(&fil, AccStringLength);
63                 //DELAY_US(100);
64             }
65         }
66     }
67 }
68
69 // Step 5. User specific code, enable __interrupts:
70
71 // Enable CPU INT4 which is connected to ECAP1-4 INT:
72 IER |= MINT4;
73
74 // Enable eCAP INTn in the PIE: Group 3 __interrupt 1-6
75 PieCtrlRegs.PIEIER4.bit.INTx1 = 1;
76
77 // Enable global Interrupts and higher priority real-time debug events:
78 EINT;
79 ERIM;
80
81 }
82
83 void InitECapture()
84 {
85     ECap1Regs.ECEINT.all = 0x0000;      // Disable all capture
86     __interrupts
87     ECap1Regs.ECCLR.all = 0xFFFF;      // Clear all CAP __interrupt
88     flags
89     ECap1Regs.ECCTL1.bit.CAPLDEN = 0;    // Disable CAP1-CAP4 register
90     loads
91     ECap1Regs.ECCTL2.bit.TSCTRSTOP = 0; // Make sure the counter is
92     stopped
93
94     // Configure peripheral registers
95     // *ECap1Regs.ECCTL2.bit.CONT_ONESHT = 1; // One-shot
96     ECap1Regs.ECCTL2.bit.CONT_ONESHT = 0; // Continuous
97     ECap1Regs.ECCTL2.bit.STOP_WRAP = 3; // Stop at 4 events in one-
98     shot mode (wrap after EVT4 in cont. mode)
99     ECap1Regs.ECCTL2.bit.CAP_APWM = 0;

```

```

95 // Capture event 1/2/3/4 polarity select
96 ECap1Regs.ECCTL1.bit.CAP1POL = 0; // Rising edge
97 ECap1Regs.ECCTL1.bit.CAP2POL = 0; // Rising edge
98 ECap1Regs.ECCTL1.bit.CAP3POL = 0; // Rising edge
99 ECap1Regs.ECCTL1.bit.CAP4POL = 0; // Rising edge
100 // Reset counter after Event 1/2/3/4 time-stamp has been captured
101 ECap1Regs.ECCTL1.bit.CTRRST1 = 1; // Difference operation
102 ECap1Regs.ECCTL1.bit.CTRRST2 = 1; // Difference operation
103 ECap1Regs.ECCTL1.bit.CTRRST3 = 1; // Difference operation
104 ECap1Regs.ECCTL1.bit.CTRRST4 = 1; // Difference operation
105
106 ECap1Regs.ECCTL1.bit.PRESCALE = 0;
107
108 ECap1Regs.ECCTL2.bit.SYNCLLEN = 0; // Disable sync in
109 ECap1Regs.ECCTL2.bit.SYNCO_SEL = 2;
110 ECap1Regs.ECCTL1.bit.CAPLDEN = 1; // Enable capture units
111
112 ECap1Regs.ECCTL2.bit.TSCTRSTOP = 1; // Start Counter
113 // *ECap1Regs.ECCTL2.bit.REARM = 1; // arm one-shot
114 ECap1Regs.ECCTL2.bit.REARM = 0;
115
116 ECap1Regs.ECCTL1.bit.CAPLDEN = 1; // Enable CAP1-CAP4 register loads
    (at capture event time)
117
118 // ECap1Regs.ECEINT.bit.CEVT4 = 1; // 4 events = __interrupt
119 ECap1Regs.ECEINT.bit.CEVT1 = 1; // EVT1=__interrupt
120 }
121
122 void spi_init()
123 {
124     SpiaRegs.SPICCR.all = 0x0007; // Reset on, rising edge, 8-bit char
        bits, loop back disabled
125     SpiaRegs.SPICTL.all = 0x0006; // Enable master mode, normal phase,
        // enable talk, and SPI int disabled (
126         b00110)
127     SpiaRegs.SPIBRR.all = 0x0063;
128     SpiaRegs.SPICCR.bit.SPISWRESET = 1; // Relinquish SPI from Reset
129     SpiaRegs.SPIPRI.bit.FREE = 1;
130 }
131
132
133 __interrupt void ecap1_isr(void)
134 {
135     diff_array[index++] = ECap1Regs.CAP1;
136     diff_array[index++] = ECap1Regs.CAP2;
137     diff_array[index++] = ECap1Regs.CAP3;
138     diff_array[index++] = ECap1Regs.CAP4;
139
140     ECap1IntCount++;
141
142     if (index == 2560)

```

```

143     {
144         if ( res == FR_OK )
145         {
146             res = f_write(&fil , diff_array , index , &bw);
147             WriteCount++;
148             AccStringLength = AccStringLength + index;
149             index = 0;
150         }
151     }
152
153     // Acknowledge this interrupt to receive more interrupts from group 4
154     PieCtrlRegs.PIEACK.all = PIEACK_GROUP4;
155 }

```

Appendix B mmc.c

```

1  /*-----*/
2  /* MMC/SDC (in SPI mode) control module (C)ChaN, 2007 */
3  /*-----*/
4  /* Only rcvr_spi(), xmit_spi(), disk_timerproc() and some macros */
5  /* are platform dependent. */
6  /*-----*/
7
8  /*
9   * This file was modified from a sample available from the FatFs
10  * web site.
11  * Works with TI TMS320F28377S.
12  */
13
14  #include "F28x_Project.h"
15
16  #include "third_party/fatfs/src/diskio.h"
17  #include "third_party/fatfs/src/integer.h"
18
19  /* Definitions for MMC/SDC command */
20  #define CMD0      (0x40+0)    /* GO_IDLE_STATE */
21  #define CMD1      (0x40+1)    /* SEND_OP_COND */
22  #define CMD8      (0x40+8)    /* SEND_IF_COND */
23  #define CMD9      (0x40+9)    /* SEND_CSD */
24  #define CMD10     (0x40+10)   /* SEND_CID */
25  #define CMD12     (0x40+12)   /* STOP_TRANSMISSION */
26  #define CMD16     (0x40+16)   /* SET_BLOCKLEN */
27  #define CMD17     (0x40+17)   /* READ_SINGLE_BLOCK */
28  #define CMD18     (0x40+18)   /* READ_MULTIPLE_BLOCK */
29  #define CMD23     (0x40+23)   /* SET_BLOCK_COUNT */
30  #define CMD24     (0x40+24)   /* WRITE_BLOCK */
31  #define CMD25     (0x40+25)   /* WRITE_MULTIPLE_BLOCK */
32  #define CMD41     (0x40+41)   /* SEND_OP_COND (ACMD) */
33  #define CMD55     (0x40+55)   /* APP_CMD */
34  #define CMD58     (0x40+58)   /* READ_OCR */
35

```

```

36 // asserts the CS pin to the card
37 static
38 void SELECT (void)
39 {
40     // Select the SD card.
41     EALLOW;
42     GpioDataRegs.GPACLEAR.bit.GPIO19 = 1; //Writing a 1 will force GPIO
output data latch to 0.
43     EDIS;
44
45 }
46
47 // De-asserts the CS pin to the card.
48 static
49 void DESELECT (void)
50 {
51     EALLOW;
52     GpioDataRegs.GPASET.bit.GPIO19 = 1; //Writing a 1 will force GPIO
output data latch to 1.
53     EDIS;
54 }
55
56 /*-----*/
57     Module Private Functions
58 /*-----*/
59
60 static volatile
61 DSTATUS Stat = STA_NOINIT;    /* Disk status */
62
63 static volatile
64 BYTE Timer1, Timer2;    /* 100Hz decrement timer */
65
66 static
67 BYTE CardType;          /* b0:MMC, b1:SDC, b2:Block addressing */
68
69 static
70 BYTE PowerFlag = 0;    /* indicates if "power" is on */
71
72 /*-----*/
73 /* Transmit a byte to MMC via SPI (Platform dependent) */
74 /*-----*/
75
76 static
77 void xmit_spi (BYTE dat)
78 {
79     volatile DWORD rcvdat;
80
81     while(SpiaRegs.SPISTS.bit.BUFFULLFLAG); //Wait for room to write
data, 0=transmit buffer not full
82     SpiaRegs.SPITXBUF = ((DWORD)dat)<<8; //Writes to SPITXBUF must be
left-justified

```

```

83
84     /* flush data read during the write */
85     while(SpiaRegs.SPISTS.bit.INT_FLAG !=1);
86     rcvdat = (SpiaRegs.SPIRXBUF && 0xFF); //Clear Receive Buffer
87 }
88
89
90 /*-----*/
91 /* Receive a byte from MMC via SPI (Platform dependent) */
92 /*-----*/
93
94 static
95 BYTE rcvr_spi (void)
96 {
97     volatile DWORD rcvdat;
98
99     /* write dummy data */
100    while(SpiaRegs.SPISTS.bit.BUFFULLFLAG); //Wait for space to write
101    SpiaRegs.SPITXBUF = 0xFF00; //Write dummy data
102
103    /* read data from RX fifo */
104    while(SpiaRegs.SPISTS.bit.INT_FLAG !=1);
105    rcvdat = (SpiaRegs.SPIRXBUF & 0xFF); //Read Transferred data
106
107    return (BYTE)rcvdat;
108 }
109
110
111 static
112 void rcvr_spi_m (BYTE *dst)
113 {
114     *dst = rcvr_spi();
115 }
116
117 /*-----*/
118 /* Wait for card ready */
119 /*-----*/
120
121 static
122 BYTE wait_ready (void)
123 {
124     BYTE res;
125
126
127     Timer2 = 50; /* Wait for ready in timeout of 500ms */
128     rcvr_spi();
129     do{
130         res = rcvr_spi();
131         DELAY_US(175);
132     } while ((res != 0xFF) && Timer2);
133

```

```

134     return res;
135 }
136
137 /*-----*/
138 /* Power Control (Platform dependent) */
139 /*-----*/
140 /* When the target system does not support socket power control, there
141    */
142 /* is nothing to do in these functions and chk_power always returns 1.
143    */
144
145 static
146 void power_off (void)
147 {
148     PowerFlag = 0;
149 }
150
151 static
152 int chk_power(void) /* Socket power state: 0=off, 1=on */
153 {
154     return PowerFlag;
155 }
156
157 /*-----*/
158 /* Receive a data packet from MMC */
159 /*-----*/
160
161 static
162 BOOL rcvr_datablock (
163     BYTE *buff, /* Data buffer to store received data */
164     UINT btr /* Byte count (must be even number) */
165 )
166 {
167     BYTE token;
168
169     Timer1 = 10;
170     do /* Wait for data packet in timeout of 100ms */
171     {
172         token = rcvr_spi();
173     }
174     while ((token == 0xFF) && Timer1);
175     if(token != 0xFE) return FALSE; /* If not valid data token, return
176    with error */
177
178     do /* Receive the data block into
179    buffer */
180     {
181         rcvr_spi_m(buff++);
182         rcvr_spi_m(buff++);
183     }

```

```

181     while (btr --= 2);
182     rcvr_spi();          /* Discard CRC */
183     rcvr_spi();
184
185     return TRUE;        /* Return with success */
186 }
187
188 /*----- */
189 /* Send a data packet to MMC */
190 /*----- */
191
192 #if _READONLY == 0
193 static
194 BOOL xmit_datablock (
195     const BYTE *buff,    /* 512 byte data block to be transmitted */
196     BYTE token           /* Data/Stop token */
197 )
198 {
199     //BYTE resp, wc;
200     BYTE resp;
201     Uint16 j;
202
203
204     //if (wait_ready() != 0xFF) return FALSE;
205     do{
206         resp = rcvr_spi();
207     }while (resp!=0xFF); // To make sure Data out line is high (SD is
not busy)
208
209     xmit_spi(token);          /* Xmit data token (0xFE for block
write)*/
210     if (token != 0xFD)        /* Is data token */ /*#define
MULTIPLE_STOP_TRANSMISSION 0xFD00*/
211     {
212         for(j=0;j<512;j++)
213             xmit_spi(*buff++); /* Xmit the 512 byte data block to MMC */
214
215         j=0;
216
217         xmit_spi(0xFF);      /* CRC (Dummy) */
218         xmit_spi(0xFF);
219
220         resp = rcvr_spi(); /* Receive data response */
221         //if ((resp & 0x0F) != 0x05 || (resp & 0x0F) != 0x02) /* If not
accepted, return with error */
222         //if ((resp & 0x0F) == 0x0B || (resp & 0x0F) == 0x0D)
223         //while ((resp & 0x1F) != 0x05){
224             //resp = rcvr_spi();
225             if( ( (resp & 0x1F) == 0x0B) || ( (resp & 0x0F) == 0x1D) )
226                 return FALSE;
227

```

```

228         do{
229             resp = rcvr_spi();
230             }while (resp!=0xFF);
231     }
232
233     return TRUE;
234 }
235 #endif /* _READONLY */
236
237 /*-----*/
238 /* Send a command packet to MMC */
239 /*-----*/
240
241 static
242 BYTE send_cmd (
243     BYTE cmd,          /* Command byte */
244     DWORD arg          /* Argument */
245 )
246 {
247     BYTE n, res;
248
249
250     if (wait_ready() != 0xFF) return 0xFF;
251
252     /* Select the card */
253     DESELECT();
254     rcvr_spi();
255     SELECT();
256     rcvr_spi();
257
258     /* Send command packet */
259     xmit_spi(cmd);          /* Command */
260     xmit_spi((BYTE)(arg >> 24)); /* Argument [31..24] */
261     xmit_spi((BYTE)(arg >> 16)); /* Argument [23..16] */
262     xmit_spi((BYTE)(arg >> 8)); /* Argument [15..8] */
263     xmit_spi((BYTE)arg);      /* Argument [7..0] */
264     //n = 0;
265     n=0;
266     if (cmd == CMD0) n = 0x95; /* CRC for CMD0(0) */
267     if (cmd == CMD8) n = 0x87; /* CRC for CMD8(0x1AA) */
268     xmit_spi(n);
269
270     /* Receive command response */
271     if (cmd == CMD12) rcvr_spi(); /* Skip a stuff byte when stop reading
272     */
273     n = 10; /* Wait for a valid response in
274     timeout of 10 attempts */
275     do{
276         res = rcvr_spi();
277     }while ((res & 0x80) && --n);
278

```



```

277     return res;                /* Return with the response value */
278 }
279
280 /*


---


281 * Send the special command used to terminate a multi-sector read.
282 *
283 * This is the only command which can be sent while the SDCard is
284 * sending
285 * data. The SDCard spec indicates that the data transfer will stop 2
286 * bytes
287 * after the 6 byte CMD12 command is sent and that the card will then
288 * send
289 * 0xFF for between 2 and 6 more bytes before the R1 response byte.
290 * This
291 * response will be followed by another 0xFF byte. In testing, however,
292 * it
293 * seems that some cards don't send the 2 to 6 0xFF bytes between the
294 * end of
295 * data transmission and the response code. This function, therefore,
296 * merely
297 * reads 10 bytes and, if the last one read is 0xFF, returns the value
298 * of the
299 * latest non-0xFF byte as the response code.
300 *
301 *


---


302 */
303
304 static
305 BYTE send_cmd12 (void)
306 {
307     BYTE n, res, val;
308
309     /* For CMD12, we don't wait for the card to be idle before we send
310      * the new command.
311      */
312
313     /* Send command packet – the argument for CMD12 is ignored. */
314     xmit_spi(CMD12);
315     xmit_spi(0);
316     xmit_spi(0);
317     xmit_spi(0);
318     xmit_spi(0);
319     xmit_spi(0);
320
321     /* Read up to 10 bytes from the card, remembering the value read if
322      * it's
323      * not 0xFF */
324     for(n = 0; n < 10; n++)

```

```

315     {
316         val = rcvr_spi();
317         if(val != 0xFF)
318         {
319             res = val;
320         }
321     }
322
323     return res;          /* Return with the response value */
324 }
325
326 /*-----
327     Public Functions
328 -----*/
329
330 /*-----*/
331 /* Initialize Disk Drive */
332 /*-----*/
333
334 DSTATUS disk_initialize (
335     BYTE drv          /* Physical drive number (0) */
336 )
337 {
338     BYTE n, ty, ocr[4];
339
340     if (drv) return STA_NOINIT;          /* Supports only single drive
341     */
342     if (Stat & STA_NODISK) return Stat;  /* No card in the socket */
343
344     //power_on();                        /* Force socket power on */
345     //send_initial_clock_train();
346
347     EALLOW;
348     //Set LSPCLK=SYSCLK/8, so that SPI Baud Rate= 200MHz/8/(0x63+1)=250
349     kHz
350     ClkCfgRegs.LOSPCP.all = 0x00000004; //Tech Ref P279
351     EDIS;
352
353     DESELECT();
354     for (n = 10; n; n--)
355         rcvr_spi(); /* 80 dummy clocks with CS=H */
356
357     //SELECT();                          /* CS = L */
358
359     ty = 0;
360     if (send_cmd(CMD0, 0) == 1)          /* Enter Idle state */
361     {
362         Timer1 = 100;                   /* Initialization timeout
363         of 1000 msec */
364         if (send_cmd(CMD8, 0x1AA) == 1)  /* SDC Ver2+ */
365         {

```

```

363         for (n = 0; n < 4; n++) ocr[n] = rcvr_spi();
364         if (ocr[2] == 0x01 && ocr[3] == 0xAA) /* The card can
work at vdd range of 2.7-3.6V */
365             {
366                 do
367                 {
368                     if (send_cmd(CMD55, 0) <= 1 && send_cmd(CMD41, 1UL
<< 30) == 0) break; /* ACMD41 with HCS bit */
369                 }
370                 while (Timer1);
371                 if (Timer1 && send_cmd(CMD58, 0) == 0) /* Check CCS
bit */
372                 {
373                     for (n = 0; n < 4; n++) ocr[n] = rcvr_spi();
374                     ty = (ocr[0] & 0x40) ? 6 : 2;
375                 }
376             }
377         }
378         else /* SDC Ver1 or MMC */
379         {
380             ty = (send_cmd(CMD55, 0) <= 1 && send_cmd(CMD41, 0) <= 1) ?
2 : 1; /* SDC : MMC */
381             do
382             {
383                 if (ty == 2)
384                 {
385                     if (send_cmd(CMD55, 0) <= 1 && send_cmd(CMD41, 0) ==
0) break; /* ACMD41 */
386                 }
387                 else
388                 {
389                     if (send_cmd(CMD1, 0) == 0) break;
/* CMD1 */
390                 }
391             }
392             while (Timer1);
393             if (!Timer1 || send_cmd(CMD16, 512) != 0) /* Select R/W
block length */
394                 ty = 0;
395         }
396     }
397     CardType = ty;
398     DESELECT(); /* CS = H */
399     rcvr_spi(); /* Idle (Release DO) */
400
401     if (ty) /* Initialization succeeded */
402     {
403         Stat &= ~STA_NOINIT; /* Clear STA_NOINIT */
404         EALLOW;
405         ClkCfgRegs.LOSPCP.all = 0x00000001;
406         SpiaRegs.SPIBRR.all = 0x0003;

```

```

407     EDIS;
408 }
409 else          /* Initialization failed */
410 {
411     power_off();
412 }
413
414 return Stat;
415 }
416
417 /*
418  */
419 /* Get Disk Status          */
420
421 DSTATUS disk_status (
422     BYTE drv          /* Physical drive number (0) */
423 )
424 {
425     if (drv) return STA_NOINIT;          /* Supports only single drive */
426     return Stat;
427 }
428
429 /*-----*/
430 /* Read Sector(s)          */
431 /*-----*/
432
433 DRESULT disk_read (
434     BYTE drv,          /* Physical drive number (0) */
435     BYTE *buff,        /* Pointer to the data buffer to store read
data */
436     DWORD sector,      /* Start sector number (LBA) */
437     BYTE count         /* Sector count (1..255) */
438 )
439 {
440     if (drv || !count) return RES_PARERR;
441     if (Stat & STA_NOINIT) return RES_NOTRDY;
442
443     if (!(CardType & 4)) sector *= 512; /* Convert to byte address if
needed */
444
445     SELECT();          /* CS = L */
446
447     if (count == 1)    /* Single block read */
448     {
449         if ((send_cmd(CMD17, sector) == 0) /* READ_SINGLE_BLOCK */
450             && rcvr_datablock(buff, 512))
451             count = 0;
452     }
453     else                /* Multiple block read */

```

```

454 {
455     if (send_cmd(CMD18, sector) == 0)      /* READ_MULTIPLE_BLOCK */
456     {
457         do
458         {
459             if (!rcvr_datablock(buff, 512)) break;
460             buff += 512;
461         }
462         while (--count);
463         send_cmd12();                      /* STOP_TRANSMISSION */
464     }
465 }
466
467 DESELECT();                               /* CS = H */
468 rcvr_spi();                               /* Idle (Release DO) */
469
470 return count ? RES_ERROR : RES_OK;
471 }
472
473 /*-----*/
474 /* Write Sector(s) */
475 /*-----*/
476
477 #if _READONLY == 0
478 DRESULT disk_write (
479     BYTE drv,                               /* Physical drive number (0) */
480     const BYTE *buff,                       /* Pointer to the data to be written */
481     DWORD sector,                           /* Start sector number (LBA) */
482     BYTE count                               /* Sector count (1..255) */
483 )
484 {
485     if (drv || !count) return RES_PARERR;
486     if (Stat & STA_NOINIT) return RES_NOTRDY;
487     if (Stat & STA_PROTECT) return RES_WRPRT;
488
489     if (!(CardType & 4)) sector *= 512;    /* Convert to byte address if
490     needed */                               //if CardType!=4
491
492     SELECT();                               /* CS = L */
493
494     if (count == 1)                          /* Single block write */
495     {
496         //if ((send_cmd(CMD24, sector) == 0) /* WRITE_BLOCK */
497         //    && xmit_datablock(buff, 0xFE))
498         if (send_cmd(CMD24, sector) == 0)
499         {
500             rcvr_spi(); //After receiving response clock must be active for
501             8 clock cycles
502             if (xmit_datablock(buff, 0xFE) == 1)
503                 count = 0;
504         }
505     }

```

```

503     }
504     else /* Multiple block write */
505     {
506         if (CardType & 2)
507         {
508             send_cmd(CMD55, 0); //CMD55=0x77, APP_CMD
509             send_cmd(CMD23, count); /* ACMD23 */ //CMD23=0x57,
SET_BLOCK_COUNT
510         }
511         if (send_cmd(CMD25, sector) == 0) /* WRITE_MULTIPLE_BLOCK
*/ //CMD25=0x59
512         {
513             rcvr_spi(); //After receiving response clock must be active
for 8 clock cycles
514             do
515             {
516                 if (!xmit_datablock(buff, 0xFC)) break;
517                 buff += 512;
518             }
519             while (--count);
520             if (!xmit_datablock(0, 0xFD)) /* STOP_TRAN token */
521                 count = 1;
522         }
523     }
524
525     rcvr_spi(); /* 8 Clk Cycles */
526     //sd_send_status();
527     if (send_cmd(0x4D, 0) != 0x00) {
528         //rcvr_spi();
529         count = 1;
530     }
531
532     DESELECT(); /* CS = H */
533     while (rcvr_spi() != 0xFF)
534         rcvr_spi(); /* Idle (Release DO) */
535
536     return count ? RES_ERROR : RES_OK; //if count=0, return RES_OK
537 }
538 #endif /* _READONLY */
539
540 /*-----*/
541 /* Miscellaneous Functions */
542 /*-----*/
543
544 DRESULT disk_ioctl (
545     BYTE drv, /* Physical drive number (0) */
546     BYTE ctrl, /* Control code */
547     void *buff /* Buffer to send/receive control data */
548 )
549 {
550     DRESULT res;

```

```

551 BYTE n, csd[16], *ptr = buff;
552 WORD csize;
553
554
555 if (drv) return RES_PARERR;
556
557 res = RES_ERROR;
558
559 if (ctrl == CTRLPOWER)
560 {
561     switch (*ptr)
562     {
563     case 0: /* Sub control code == 0 (POWER.OFF) */
564         if (chk_power())
565             power_off(); /* Power off */
566         res = RES_OK;
567         break;
568     case 1: /* Sub control code == 1 (POWER.ON) */
569         power_on(); /* Power on */
570         res = RES_OK;
571         break;
572     case 2: /* Sub control code == 2 (POWER.GET) */
573         *(ptr+1) = (BYTE)chk_power();
574         res = RES_OK;
575         break;
576     default :
577         res = RES_PARERR;
578     }
579 }
580 else
581 {
582     if (Stat & STA_NOINIT) return RES_NOTRDY;
583
584     SELECT(); /* CS = L */
585
586     switch (ctrl)
587     {
588     case GET_SECTOR_COUNT : /* Get number of sectors on the disk
589 (DWORD) */
590         if ((send_cmd(CMD9, 0) == 0) && rcvr_datablock(csd, 16))
591         {
592             if ((csd[0] >> 6) == 1) /* SDC ver 2.00 */
593             {
594                 csize = csd[9] + ((WORD)csd[8] << 8) + 1;
595                 *(DWORD*)buff = (DWORD)csize << 10;
596             }
597             else /* MMC or SDC ver 1.XX */
598             {
599                 n = (csd[5] & 15) + ((csd[10] & 128) >> 7) + ((csd
[9] & 3) << 1) + 2;
600                 csize = (csd[8] >> 6) + ((WORD)csd[7] << 2) + ((WORD

```

```

600     )(csd[6] & 3) << 10) + 1;
601         *(DWORD*) buff = (DWORD) csize << (n - 9);
602     }
603     res = RES_OK;
604 }
605 break;
606 case GET_SECTOR_SIZE :    /* Get sectors on the disk (WORD) */
607     *(WORD*) buff = 512;
608     res = RES_OK;
609     break;
610 case CTRL_SYNC :        /* Make sure that data has been written */
611     if (wait_ready() == 0xFF)
612         res = RES_OK;
613     break;
614 case MMC_GET_CSD :      /* Receive CSD as a data block (16 bytes)
615 */
616     if (send_cmd(CMD9, 0) == 0          /* READ_CSD */
617         && rcvr_datablock(ptr, 16))
618         res = RES_OK;
619     break;
620 case MMC_GET_CID :      /* Receive CID as a data block (16 bytes)
621 */
622     if (send_cmd(CMD10, 0) == 0        /* READ_CID */
623         && rcvr_datablock(ptr, 16))
624         res = RES_OK;
625     break;
626 case MMC_GET_OCR :      /* Receive OCR as an R3 resp (4 bytes) */
627     if (send_cmd(CMD58, 0) == 0        /* READ_OCR */
628         {
629         for (n = 0; n < 4; n++)
630             *ptr++ = rcvr_spi();
631         res = RES_OK;
632     }
633 }
634 // case MMC_GET_TYPE :    /* Get card type flags (1 byte) */
635 //     *ptr = CardType;
636 //     res = RES_OK;
637 //     break;
638 //
639 //
640 default :
641     res = RES_PARERR;
642 }
643
644 DESELECT();          /* CS = H */
645 rcvr_spi();         /* Idle (Release DO) */
646 }
647

```



```

648
649     return res;
650 }
651
652 /*-----*/
653 /* User Provided Timer Function for FatFs module */
654 /*-----*/
655 /* This is a real time clock service to be called from */
656 /* FatFs module. Any valid time must be returned even if */
657 /* the system does not support a real time clock. */
658
659 DWORD get_fattime (void)
660 {
661
662     return    ((2008UL-1980) << 25)    // Year = 2008
663             | (2UL << 21)              // Month = February
664             | (26UL << 16)             // Day = 26
665             | (14U << 11)              // Hour = 14
666             | (0U << 5)                // Min = 0
667             | (0U >> 1)                // Sec = 0
668             ;
669
670 }

```

Appendix C datatranslate.py

```

1 #!/usr/bin/python
2
3 f = open("/Users/xiaoyu/Downloads/LOG.txt", "r")
4 fo = open("/Users/xiaoyu/Downloads/out.LOG.txt", "w+")
5
6 RawData = list(f.read())
7
8 TranData = []
9
10 for data in RawData:
11     if ord(data) != 0 and ord(data) != 13:
12         TranData.append(str(ord(data)))
13         fo.write(str(ord(data))+ " ")

```